



Ahmed Zabana University Center of Relizane



Industrial Engineering and Sustainable Development Laboratory.

**Revue
des Matériaux
&
Energies Renouvelables**

ISSN-Online: 2661-7595

Volume 4, Issue 2 (March 2021)



Reacherch Review of Sciences and Technologies

Sommaire:

Assessment of thermal comfort in some public buildings in the sudano-sahelian area of Cameroon during the so-called "cold" period (harmattan season).....1

Lissangadi MOUNOUNA DAPSIA¹, Ahmat TOM², Noël DJONGYANG^{1*}

Simulation et optimisation de l'épaisseur de l'émetteur d'une cellule solaire mono-jonction à base de GaAs.....17

H.CHARANE1,* , A .MAHRANE2, A. MESRANE3 et H.MAZOUZ4

Une nouvelle théorie quasi-3D de déformation de cisaillement pour l'analyse statique des poutres stratifiées à couches croisées symétriques et antisymétriques en matériaux non homogènes.....23

KADDARI Miloud 1,* , KAÇI Abdelhakim 1,2, TOUNSI Abdelouahed 1

Reliable Standalone Solar Battery Charging System Using ARDUINO Based on MPPT Controller.....33

Seddik ZEMITTE 1*, Messaoud HAMOUDA 1, Fatima Zohra ARAMA 1, Ahmed SAIDI 2

Magnetic investigation of the rhodium based full-heusler material: ab initio Method43

BOUFADI Fatima Zohra^{1*}

Editorial:

This issue presents articles that illustrate the diversity of research activity and development carried out on materials and renewable energies, and reflect the spirit with which we find the fruits of our researchers and PhD students. Our goal is to federate scientific actions on materials and renewable energies to ensure a link between the academic and industrial communities.

Prof. MAHMOUDI. N

Editorial:

Ce numéro présente des articles qui illustrent la diversité d'activité de recherche et de développement menés sur les matériaux et les énergies renouvelables, et reflètent bien l'esprit avec lequel l'on trouve les fruits de nos chercheurs et thésards. Notre but est de fédérer les actions scientifiques sur les matériaux et les énergies renouvelables pour assurer un lien entre les communautés académiques et industrielles.

Prof. MAHMOUDI. N



**Revue des Matériaux
&
Energies Renouvelables**

Journal home : www.cu-relizane.dz

ISSN : 2507-7554

E- ISSN : 2661-7595



Assessment of thermal comfort in some public buildings in the sudano-sahelian area of Cameroon during the so-called "cold" period (harmattan season)

Open Access

Lissangadi Mounouna Dapsia¹, Ahmat Tom², Noël Djongyang^{1*}

¹ Department of Renewable Energy, National Advanced School of Engineering of Maroua, University of Maroua, PO Box 46 Maroua, Cameroon

² Department of Energy Engineering, University Institute of Technology, University of Ngaoundere, PO Box 455 Ngaoundere, Cameroon

ABSTRACT

This paper deals with adaptive thermal comfort in public buildings in the Sudano-Sahelian zone of Cameroon during the harmattan season. In-situ data measurements were taken in various buildings according to the type of landforms (mountain and plain). A quantitative sociological survey was also conducted on the thermal sensation of the occupants. The Predicted Mean Vote and Predicted Percentage of Dissatisfied comfort indexes were evaluated as well as the Actual Mean Vote, and the Actual Percentage of Dissatisfied. Results showed that the operative temperatures and the relative humidity determined on the basis of the Actual Mean Vote were respectively 20.09 °C and 30.35 % (in the Mountains), 20.92 °C and 61.94 % (in plains). The operative temperatures of the comfort zone in the mountain area were between 14.20 °C and 22.45 °C while the operative temperatures of the comfort zone in the plain zone are between 17.5 °C and 24.3 °C. Occupants testified indoor "thermal unacceptability" especially for public administrations and schools.

Article history:

Received 11 July 2020

Received in revised form 31 July 2020

Accepted 20 August 2020

Keys word: Public buildings; Sudano-Sahelian zone; Thermal comfort; Harmattan season; Thermal acceptability; Neutral operative temperature

Copyright © 2020 - All rights reserved

1. Introduction

Most of the time, buildings are just considered as a shelter. Therefore, some aspects related to internal thermal comfort are not taken into account in the architectural design; consequently, they may not be well adapted for some specific areas.

Thermal comfort is defined according to the ASHRAE standard 55 as the condition of the mind which expresses satisfaction with the thermal environment [1]. As such, it will be influenced by personal differences in mood, culture and other individual, organizational and social factors. Based on the above definition, comfort is not a state condition, but rather a state of mind. The definition of thermal comfort leaves open as to what is meant by condition of mind or satisfaction, but it correctly emphasizes that the judgment of comfort is a cognitive process involving many inputs influenced by physical, physiological, psychological, and other factors [2]. It has an impact on intellectual performance [3]. It is also a key parameter for a healthy and productive workplace (shopping centres, administrative offices, worship places, etc.). Thermal comfort standards determine the energy consumption by a building's environmental systems; therefore, they play an important role in building sustainability. Hence, it is essential to think of adopting public buildings suitable for the climate

* Corresponding author. E-mail address: noeldjongyang@gmail.com

of the Sudano-Sahelian zones, in order to improve the level of their thermal comfort. Thermal comfort depends on parameters like air temperature, relative air humidity, air speed, metabolism, clothing, etc. These parameters are used to determine the thermal sensation based on the objective method (Fanger model) [4]. The thermal sensation is also determined by the subjective approach (the occupants' vote) [5].

Numerous studies based on the thermal comfort of occupants in buildings have been carried out; eg. Ionnou and Itard [6] carried out in-situ measurements of thermal comfort in 30 residential habitats in the Netherlands and compared with existing results from the literature. They proceeded with quantitative (temperature, relative humidity, etc.) and qualitative (thermal sensation and perception, clothing, measurements taken during the last half hour regarding comfort and energy consumption, etc.) measurements. The results obtained showed that the PMV model underestimates the thermal comfort of the tenants in houses. They also showed that clothing, metabolic activity, age and sex have no influence on the neutral temperature and that it is the speed air, adaptation and psychological expectations which are the explanatory factors for the difference in neutral temperature between habitats. Castaño et al. [7] studied the optimization of the thermal comfort of buildings under the natural ventilation regime (with focus on the facades), in order to obtain sufficient comfort levels, low energy consumption in offices subject to the Mediterranean climate. This work was based on thermal modelling and simulation for a full year and without air conditioning installation. It consisted in analysing the situation of thermal comfort inside buildings by calculating the percentage of hours of thermal comfort. The results obtained attested that the combination of natural stimulation (facade) controlled with air conditioning systems constitutes the most suitable design solution in a Mediterranean climate. In the same context, Rijal et al. [8] provided an adaptive model specifically applicable to Japanese homes and clarified the adaptation mechanism (physiological and behavioural) of the occupants. For this, thermal measurements and surveys on thermal comfort were carried out in the living room and bedrooms of 120 dwellings, including 244 residents, each with an air conditioning unit and a fan from the Kanto region of Japan from 2010 to 2014. The results obtained showed that residents are generally satisfied with the thermal environment of their homes, and that the temperature in free operating mode is around 27.6 °C in summer and 17.6 °C in winter. They also showed that an adaptive relationship between the indoor comfort temperature and the outdoor air temperature could be a useful way to estimate the comfort temperature and provide information on control strategies. Finally, they concluded that different adaptation mechanisms (behavioural adaptation, psychological adaptation) contribute significantly to the adaptive model. Roumaissa et al. [3] studied the correlation between architectural typologies of middle-school buildings and the thermal comfort of users in an area with a hot and arid climate in Algeria, more precisely in Bishar. Questionnaire surveys and in-situ measurement campaigns were carried out. The results attested that in hot weather, whatever the plan, the temperature of the rooms remains high and this is valid for the four cardinal orientations. They also found that there is a strong correlation between the ambient temperature and the thermal sensation of the students and finally that the typology of the central corridor plan offers conditions more favourable to thermal comfort. In Cameroon, Kemajou and Mba [9] worked on obtaining thermal comfort in the habitat by a judicious choice of materials in hot areas. They proceeded by thermal simulation based on the Pleiades + Comfie software and carried out a comparison between local and modern materials. The results of this study have shown that better thermal comfort is obtained with local materials based on passive methods (architectural forms, orientation, size of openings, etc.) in line with architectural habits.

Most of the studies encountered in the literature are limited in the study of thermal comfort to the determination of the neutral temperature and yet relative humidity plays a key role in thermal sensation [10-21]. In this paper, in addition to neutral temperature, we also look at the influence of neutral relative humidity on thermal comfort.

If the climate is generally quite mild in the equatorial climatic region of Cameroon, this is not the case in the Sudanese and Sudano-Sahelian climatic zones which experience peaks of temperature alternating between very hot and very cold. But generally, the climate is hot thus making cold periods particularly difficult to support by the local population. This is why it is this particularly cold period which draws our attention in this work. In this paper, we will be interested in determining the different indexes of thermal comfort (PMV, PPD, AMV, APD), and the correlations existing between them in different types of public buildings and then estimating the neutral temperature and relative neutral humidity in the two types of relief (mountain and plain) during the "cold" period. This study will allow to develop passive (architectural applications) and / or active (use of air conditioning) methods in order to optimize thermal comfort and energy consumption in public buildings in the Sudano-Sahelian zone.

2. Study area

Cameroon is situated between latitude of 2°N to 13°N, longitude of 9°E to 17°E and covers a land area of about 475 442 km² (fig. 1). An equatorial climate with four seasons (two dry and two rainy) is found in the southern part and Atlantic

Ocean coasts with approximately 3 890 mm of precipitation per year. Abundant rainfall occurs from April to November, and practically throughout the year in the south-west mountains (approximately 10 000 mm per year). The climate tends to be of the sahelian type as one leaves the southern to the northern part of the country with two seasons (one dry and one rainy). The dry season lasts from October to April (700 mm of precipitation per year in the central plateau) and the north-west is semi-arid (380 mm of precipitation per year). Three main climatic regions are found: the southern equatorial region, which extends from 2°N to nearly as far as latitude 6°N; the Sudanese region, wet and tropical, extending from 7°N to a little beyond 10°N; the sudano-sahelian region (10 - 13) °N, dry and tropical [10].

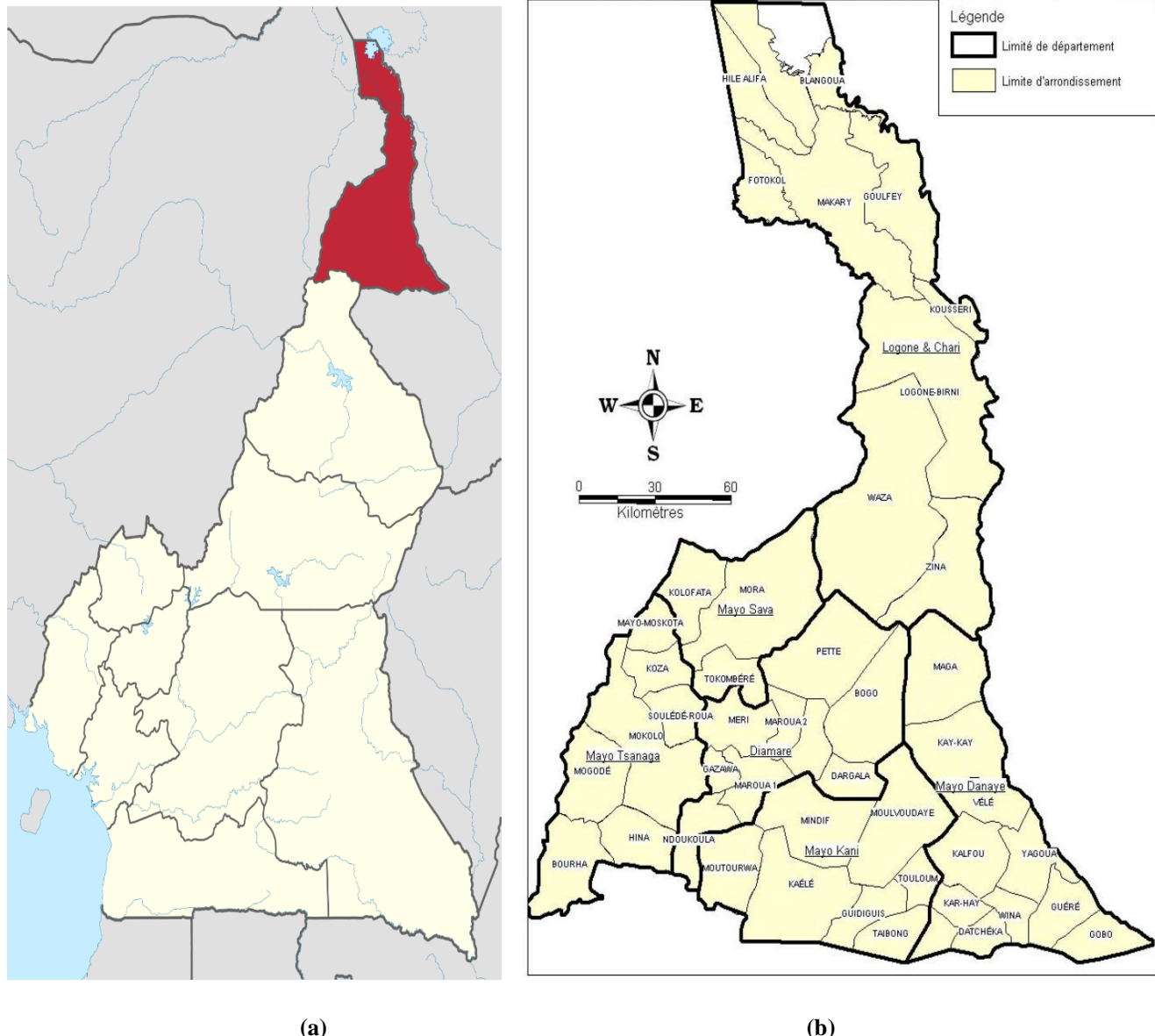


Figure 1– Cameroon map (a) outlining Far-North Region (b)

The mean outdoor temperatures vary between 25°C in the south, 21.1°C in the central plateau and 32.2°C in the north. Two climatic regions are concerned by the Harmattan wind; a cold-dry wind blowing from November to January: the Sudanese and the Sudano-Sahelian regions. The called wind dries skin, splits and wounds lips and feet, the atmosphere is foggy reducing solar radiation, low temperatures occur [10]. The study was conducted in the Far North region of Cameroon (Fig. 1). The sites chosen took into account the relief (because of some specific microclimates related to landform). We opted for mountain and plain sites. The mountainous site is made up of the following localities: Mokolo (10.7425° N, 13.8042° E), Roua (10° 47' 18" N, 14° 01' 05" E), Hina (10° 22' 7" N, 13° 51' 21"), Bourha (10.3396° N, 13.5625° E), Mogode (10.6070° N, 13.5697° E), and Mozogo (10.9624° N, 13.9042° E). The plain sites are the localities of : Koza (10.8683° N, 13.8825° E), Minawao Refugees Camp (10.5514° N, 13.8646° E), and Maroua (10.5925° N, 14.3210° E). At each site we studied three types of public buildings: administrative offices (public administration), primary and secondary schools (schools), and hotels. The study was conducted from December 26, 2019 to March 02, 2020 during working hours (10 am-2pm).

3. Methodology

The research is based on the adaptive approach which consists of two approaches:

- The objective method, which consists of taking in-situ measurements using technical instruments (measurements of ambient temperature, relative humidity, air speed, brightness, etc.) in the various buildings ;
- The subjective method, which consists of conducting quantitative or qualitative sociological surveys by questionnaire on the thermal comfort of the occupants. A questionnaire was therefore developed and administrated to the occupants in parallel with the in-situ measurements.

3.1. The Objective Method

It is based on the measurement of objective variables (ambient air temperature inside and outside, relative humidity inside and outside, air speed) according to the standard ISO 7730. We used two environmental multimeters (Digital Multimeter PM 8229 and Velleman DEM900) (figure 2).



Figure 2– Materials used during in-situ measurements : (a) Digital Multimeter PM 8229, (b) Velleman DEM900

The values collected allowed to calculate PMV (Predicated Mean Vote) and PPD (Predicated Percentage of Dissatisfied) of Fanger based on the following formulas and equations:

$$M = 0.303 \exp(0.036M - 0.028W - 3.05 \times 10^{-8} \cdot T_{cl}^4 + 733 \cdot T_{cl} \cdot 6.99 \cdot M \cdot W - P_v \cdot 0.42 \cdot f_{cl} \cdot M \cdot W - 58.15 \cdot 1.7 \cdot 10^{-5} \cdot M \cdot 867 \cdot P_v + 0.0014 \cdot M \cdot 4 \cdot T_a + 3.96 \cdot 10^{-8} \cdot f_{cl} \cdot T_{cl}^4 + 273 \cdot f_{cl} \cdot h_c \cdot T_{cl} \cdot T_a) \quad (1)$$

With:

M = activity + metabolic rate (W / m^2),

W = external work (W),

Icl = thermal resistance of clothes,

Tcl=fraction covered by clothes,

Ta = air temperature ($^{\circ}\text{C}$),

Tr = average radiant temperature ($^{\circ}\text{C}$),

Pv= partial pressure of water vapor (Pa),

hc = convective heat transfer coefficient ($\text{W} / \text{m}^2 \cdot \text{K}$),

Va = air speed (m / s).

$$Tcl = 35.7 - 0.028(M - W) - \{3.96 \times 10^{-8} \times fcl [(Tcl + 273)^4 - (Tr + 273)^4] + fcl \cdot hc [Tcl - ta]\} \quad (2)$$

$$hc = \max(2.38(Tcl - ta)^{0.25}, 12.1\sqrt{Va}) \quad (3)$$

$$Tcl \begin{cases} 1.00 + 1.290Icl & \text{if } Icl < Icl \\ 1.05 + 0.645Icl & \text{if } Icl > 0,078 \end{cases} \quad (4)$$

$$Pv = \frac{HR}{100} \exp \left(23.3265 - \frac{3802.7}{Ta+278.18} - \frac{472.68}{Ta+278.18} \right)^2 \quad (5)$$

$$PPD = 100 - 95 \exp (-0.03353PMV^4 - 0.2179PMV^2) \quad (6)$$

In the current study, we used $M = 70 \text{ W / m}^2$ (person sitting in mental work), $Icl = 1 \text{ clo}$ (clothing for the cold period) and $W = 0$.

Regarding the radiant temperature (Tr), we used the Nagano formula :

$$Tr=0.99Ta - 0.01 \quad (7)$$

and the operative temperature

$$Top=aTa + (1 - a)Tr \quad (8)$$

with $a=0.5$ if $Va \leq 0.2$ $a=0.6$ si $0.2 \leq Va \leq 0.6$ $a=0.7$ if $0.6 \leq Va \leq 1$

3.2. The subjective method

We established 143 questionnaires for the mountain sites and 112 for the plain sites, which makes a total of 255 questionnaires, all of "longitudinal" type. The questionnaire consisted of six sections, three of which related to thermal comfort: general personal information (age, sex, activity, clothing); Site (mountain, plain); Thermal comfort of the space (thermal sensation, thermal preference).

4. Results and discussions

4.1 Indoor environmental parameters

Table 1 and 2 presents respectively the data recorded during in-situ measurements, and the PMV and PPD indexes calculated according to the Fanger model. One could see that the maximum operating temperature (Top) is 37 °C, recorded in Public Administration buildings in the Mountainous area (Bourrrha) and the minimum operating temperature (Top) is 23.1 °C recorded in the plain area (Hotel Sahel of Maroua). Maximum relative humidity (Hr) is 34% and minimum is 5%. The maximum speed is 0.09 m/s recorded in the plain area (Minawao Refugee Camp) and the minimum is 0.01m/s. These values of indoor air velocity are within those recommended by the ASHRAE that it should not be greater than 0.15 m/s. From the relative humidity values, one could remark that the weather is very dry. The values of the relative humidity are far from those prescribed by the ASHRAE guidelines which recommend a relative humidity (RH) of 30 to 60 percent. This could explain the following phenomena encountered on the area : dry skins (particularly lips), eye irritation, static electricity in air, and some respiratory diseases. Table 2 shows that whatever the type of relief, the feeling of discomfort is felt by the occupants.

4.2 Actual Mean Vote (AMV).

Table 3 presents the Actual Mean Votes recorded during the measurement campaign. It could be seen that for the public administration, the AMV were $\bar{x} 0.84$ and $\bar{x} 1.27$ respectively for the mountain and plain areas while for the Schools, the AMV were $\bar{x} 1.22$ and $\bar{x} 0.82$ respectively for the mountain and plain areas. In the hotels, these values were $\bar{x} 0.95$ and $\bar{x} 0.40$ respectively for the mountain and plain areas. For the public administration, the Actual Percentage of Dissatisfied (APD) were 19.9 % and 38.73 % respectively for the mountain and plain areas while for the Schools, the APD were 36.23 % and 19.18 % respectively for the mountain and plain areas. In the hotels, these values were 24.06 % and 8.33 % respectively for the mountain and plain areas. These results confirm the overall tendency "cold" felt by the occupants during the harmattan season.

Table 1- Average values of measured data

Site	Type of Building	T_{in} (°c)	Tr (°c)	Air speed (m /s)	T_{op} (°c)
Mountainous area	Public administration	max : 37.2	max : 36.8	0.03	max : 37.0
		min : 27.3	min : 27.0	0.03	min : 27.0
		mean : 32.0	mean : 31.6	0.03	mean : 31.8
	Schools	max : 35	max : 34.6	0.02	max : 34.8
		min : 31.2	min : 30.8	0.01	min : 31.0
		mean : 33.5	mean : 33.1	0.015	mean : 33.3
	Hotel	max : 30.9	max : 30.6	0.03	max : 30.7
		min : 29.7	min : 29.4	0.03	min : 29.7
		mean : 30.4	mean : 30.0	0.03	mean : 30.2
Plain area	Public administration	max : 28.4	max : 28.1	0.03	max : 28.2
		min : 23.1	min : 22.8	0.03	min : 22.9
		mean : 24.5	mean : 24.2	0.03	mean : 24.3
	Schools	max : 27.9	max : 27.6	0.09	max : 27.7
		min : 26.5	min : 26.2	0.03	min : 26.3
		mean : 27.2	mean : 26.9	0.03	mean : 27.05
	Hotel	max : 23.6	max : 23.3	0.02	max : 23.4
		min : 23.3	min : 23.05	0.02	min : 23.1
		mean : 23.4	mean : 23.1	0.02	mean : 23.2

In-situ measurement period: December 26, 2019 - March 02, 2020, Schedule: 10 am-2pm (work hours)

Table 2- Fanger PMV and PPD calculation table

Site	Type of Building	T _{in} (°c)	Tr (°c)	Air velocity (m /s)	T _{op} (°c)	Calculated PMV	Calculated PPD (%)	Observations
Mountainous area	Public administration	max : 37.2	max : 36.8	0.03	max : 37.0	max : 5.91	max : 100	Discomfort
		min : 27.3	min : 27.0	0.03	min : 27.0	min : 4.00	min : 99	
		mean : 32.0	mean : 31.6	0.03	mean : 31.8	mean : 4.88	mean : 100	
	Schools	max : 35	max : 34.6	0.02	max : 34.8	max : 5.46	max : 100	Discomfort
		min : 31.2	min : 30.8	0.01	min : 31.0	min : 4.77	min : 100	
		mean : 33.5	mean : 33.1	0.015	mean : 33.3	mean : 5.15	mean : 100	
	Hotel	max : 30.9	max : 30.6	0.03	max : 30.7	max : 4.75	max : 100	Discomfort
		min : 29.7	min : 29.4	0.03	min : 29.7	min : 4.34	min : 100	
		mean : 30.4	mean : 30.0	0.03	mean : 30.2	mean : 4.43	mean : 100	
Plain area	Public administration	max : 28.4	max : 28.1	0.03	max : 28.2	max : 4.20	max : 99	Discomfort
		min : 23.1	min : 22.8	0.03	min : 22.9	min : 3.35	min : 99	
		mean : 24.5	mean : 24.2	0.03	mean : 24.3	mean : 3.59	mean : 99	
	Schools	max : 27.9	max : 27.6	0.09	max : 27.7	max : 4.55	max : 100	Discomfort
		min : 26.5	min : 26.2	0.03	min : 26.3	min : 3.60	min : 99	
		mean : 27.2	mean : 26.9	0.03	mean : 27.05	mean : 3.54	mean : 99	
	Hotel	max : 23.6	max : 23.3	0.02	max : 23.4	max : 2.60	max : 95	Discomfort
		min : 23.3	min : 23.05	0.02	min : 23.1	min : 2.57	min : 94	
		mean : 23.4	mean : 23.1	0.02	mean : 23.2	mean : 2.59	mean : 95	

In-situ measurement period: December 26, 2019 - March 02, 2020, Schedule: 10 am-2pm (work hours)

Table 3- AMV calculation table (Actual Mean Vote) = measured PMV**I- Mountainous area**

Public administration	ASHRAE Scale Point	-3	-2	-1	0	1	2	3
	Respondents	6	14	30	5	12	0	2
	Total number of respondents				69			
	AMV				-0.84			
	APD(%)				19.9			
School	ASHRAE Scale Point	-3	-2	-1	0	1	2	3
	Respondents	20	6	14	0	13	0	2
	Total number of respondents				55			
	AMV				-1.22			
	APD(%)				36.23			
Hotel	ASHRAE Scale Point	-3	-2	-1	0	1	2	3
	Respondents	1	3	13	0	1	0	1
	Total number of respondents				19			
	AMV				-0.95			
	APD(%)				24.06			

In-situ measurement period: December 26, 2019 - March 02, 2020, Schedule: 10 am-2pm (work hours)

II-Plain area

	ASHRAE Scale Point	-3	-2	-1	0	1	2	3
Public administration	Respondents	5	10	4	1	6	0	0
	Total number of respondents				26			
	AMV					-1.27		
	APD(%)					38.73		
Schools	ASHRAE Scale Point	-3	-2	-1	0	1	2	3
	Respondents	8	13	20	15	7	0	3
	Total number of respondents				66			
	AMV					-0.82		
	APD(%)					19.18		
Hotel	ASHRAE Scale Point	-3	-2	-1	0	1	2	3
	Respondents	0	1	13	1	4	0	1
	Total number of respondents				20			
	AMV					-0.40		
	APD(%)					8.33		

In-situ measurement period: December 26, 2019 - March 02, 2020, Schedule: 10 am-2pm (work hours)

4.3. Thermal satisfaction

The data collected permitted to assess the thermal satisfaction of the occupants according to the type of landform.

- ♦ *In the mountain area*

In mountain areas, the percentage of thermal satisfaction was 68.11 % in public administration buildings, while in educational institutions, the votes indicated a satisfaction percentage of 49.08 %. Occupants of hotels votes indicated a satisfaction percentage of 73.66 %.

- ♦ *In the plain area*

In plain areas, the percentage of thermal satisfaction was 42.29 % in public administration buildings, while in educational institutions, the vote indicates a satisfaction percentage of 63.62%. Occupants of hotels votes indicated a satisfaction percentage of 90 %.

One could therefore remark that for the two cases, the hotels are areas where we have the highest percentage of satisfaction. This could be justified by the fact that more passive techniques might have been taken into account in these cases. In fact, these areas were the most frequented tourist areas in North-Cameroon before the advent of Boko Haram terrorists and the COVID-19 health crisis. Architectural techniques were automatically integrated into most hotel establishments.

4.4 Thermal acceptability

The data collected permitted to assess the thermal satisfaction of the occupants. Results are presented in figure 3.

- ♦ *In the mountain area*

In mountain areas (Fig 3-a), the percentage of thermal acceptability was 47.8 % in public administration buildings, while in educational institutions, the vote indicates an acceptability percentage of 36.3 %. Occupants of hotels votes indicates an acceptability percentage of 78.9 %.

- ♦ *In the plain area*

In plain areas (Fig 3-b), the percentage of thermal acceptability was 57.6 % in public administration buildings, while in educational institutions, the vote indicates an acceptability percentage of 60.6 %. Occupants of hotels votes indicates an acceptability percentage of 42.2 %.

The above results shows that no type of building satisfies the conditions of ASHRAE 55-81 which stipulates that the acceptance rate for thermal comfort must exceed 80%, hence no building is considered thermally "acceptable".

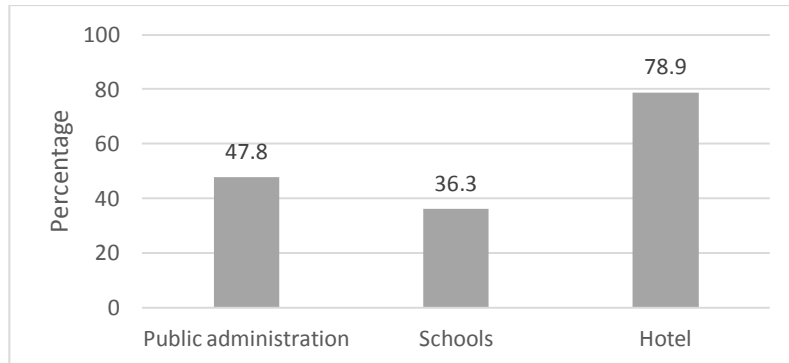


Figure 3a- Thermal acceptability (Mountainous area)

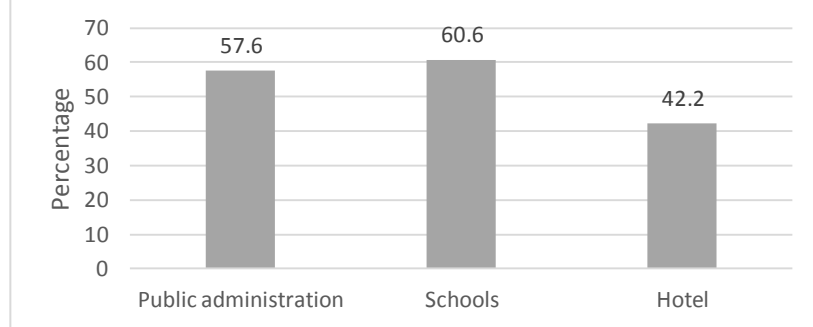


Figure 3b- Thermal acceptability (Plain area)

4.5. Thermal preference

Thermal preference was assessed directly from the questionnaire using the McIntyre's scale of thermal preference through the question "At the present time, would you prefer warmer (+1), no change (0) or cooler (-1) environment ?" Various distributions of respondents' votes are presented in figure 4.

In mountain areas (Fig. 4-a) and in the plains (Fig. 4-b), the general tendency of the occupants' preferential judgments is for "neutral" (neither hot nor cold). This is to say that the majority aspire for optimal thermal comfort.

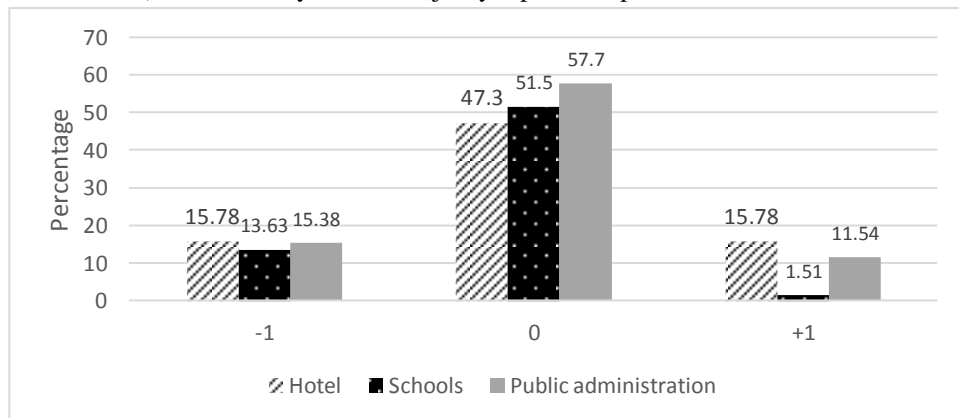


Figure 4-a : Thermal Preference - McIntyre Scale (Mountainous area)

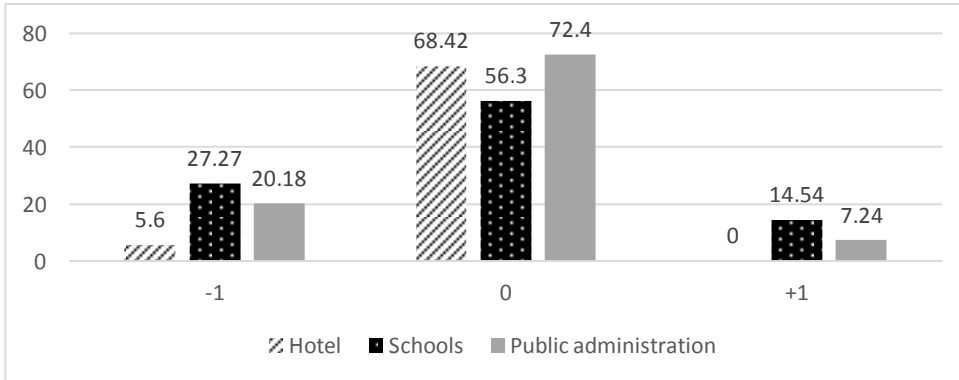


Figure 4-b : Thermal Preference - McIntyre Scale (Plain area)

4.6. PMV and thermal operative temperature

Figure 5 expresses the relationship between the PMV and the operative temperature. Fig 5-a (mountain area) and Fig 5-b (plain), give us the following linear regression:

- ♦ *Mountainous area*

$$\text{PMV}=0.196\text{Top} \bar{x} 1.387 ; R^2=0.979 \quad (9)$$

$$\text{For a PMV}=0, \text{ we have : Top}_{\text{neutral}}=7.07 \text{ }^{\circ}\text{C} \quad (10)$$

- ♦ *Plain area*

$$\text{PMV}=0.33\text{Top} \bar{x} 5.028 ; R^2=0.74 \quad (11)$$

$$\text{For a PMV}=0, \text{ we have : Top}_{\text{neutral}}=14.83 \text{ }^{\circ}\text{C} \quad (12)$$

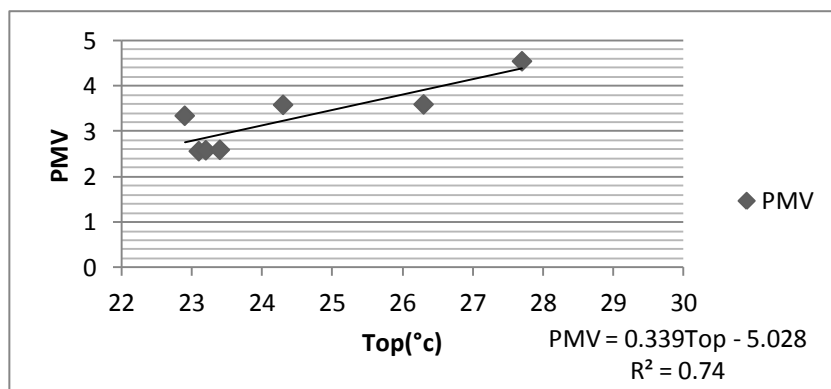


Figure 5-a : Neutral temperature (Mountainous area)

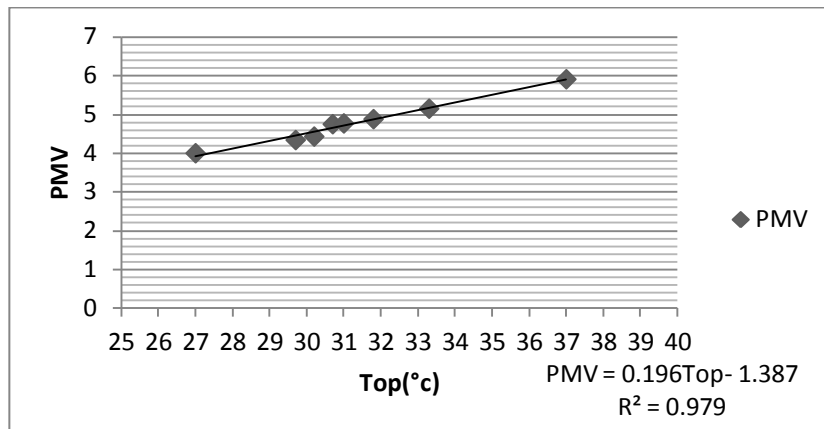


Figure 5-b : Neutral temperature (Plain area)

We can note that the PMV of Fanger does not give the correct ideal temperature, it underestimates the neutral temperature.

4.7. AMV and Neutral Operative Temperature

Figure 6 presents the relationship between the AMV and the operative temperature. Fig 6.a (mountain area) and Fig 6.b (plain) give us the following linear regression equations.

- ♦ Mountain area

$$AMV = -0.085Top + 1.708 ; R^2 = 0.458 \quad (13)$$

$$\text{For } AMV=0, \text{ we get : } Top_{\text{neutral}} = 20.09 \text{ } ^\circ\text{C} \quad (14)$$

- ♦ Plain area

$$AMV = -0.148Top + 3.097 ; R^2 = 0.811 \quad (15)$$

$$\text{For } AMV=0, \text{ we get : } Top_{\text{neutral}} = 20.92 \text{ } ^\circ\text{C} \quad (16)$$

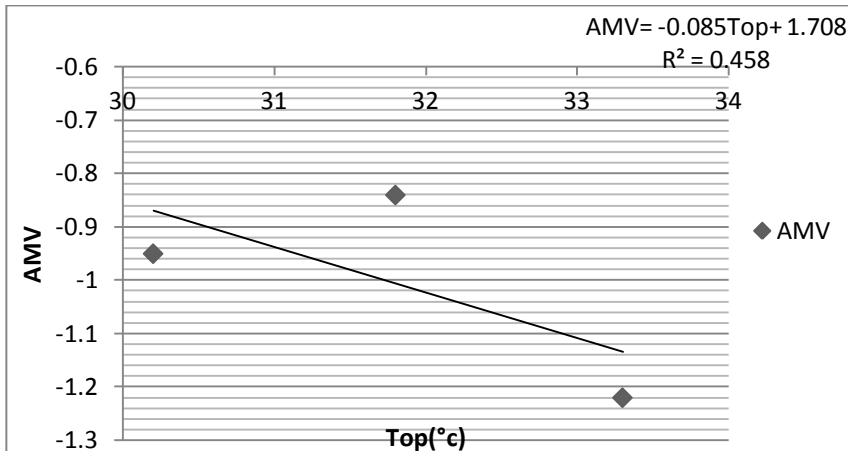


Figure 6-a : Neutral temperature(Mountainous area)

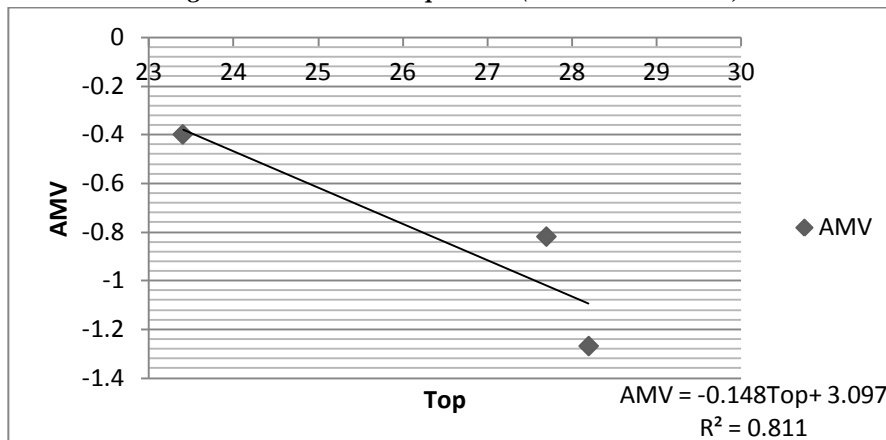


Figure 6-b : Neutral temperature (Plain area)

4.7.1 Comparison of neutral temperature to the predictions of international standards

✓ Standards ISO 7730

According to the ISO Standards 7730, for a class A comfort (high comfort class), the PPD in built environments should be less than 6 % and the ambient temperature must be between 21 °C and 23 °C in winter. From the above results, our various neutral temperatures obtained are not in line with this standard. This could be justified by the fact that even the climate is cold during the harmattan season it is better compared to the winter.

✓ Guidelines for internal climate conditions in winter (Christophe Zurcher-Thomas Franck)

According to the guidelines for internal climate conditions in winter, for offices, the temperature must be between 19 °C and 21 °C while for classrooms, the temperature must be between 19 °C and 21 °C. For hotel, the temperature must be between 19 °C and 21 °C. From the above results, one could see that our results meet these requirements.

4.8. PMV and relative humidity

Figure 7 presents the relationship between the PMV and the relative humidity. Fig 7-a (mountain area) and Fig 7-b (plain), give us the following linear regression equations:

♦ Mountainous area

$$\text{PMV} = -0.067 \text{ HR} + 5.864 ; R^2 = 0.468 \quad (17)$$

$$\text{For PMV}=0, \text{ we get : HR}_{\text{neutral}} = 87.52\% \quad (18)$$

♦ Plain area

$$\text{PMV} = -0.119 \text{ HR} + 7.371 ; R^2 = 0.489 \quad (19)$$

$$\text{For PMV}=0, \text{ we have : HR}_{\text{neutral}} = 61.94\% \quad (20)$$

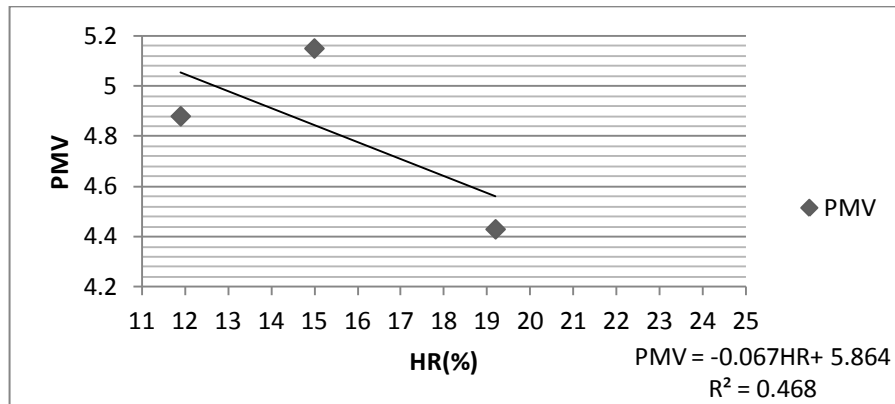


Figure 7-a : Neutral relative humidity(Mountainous area)

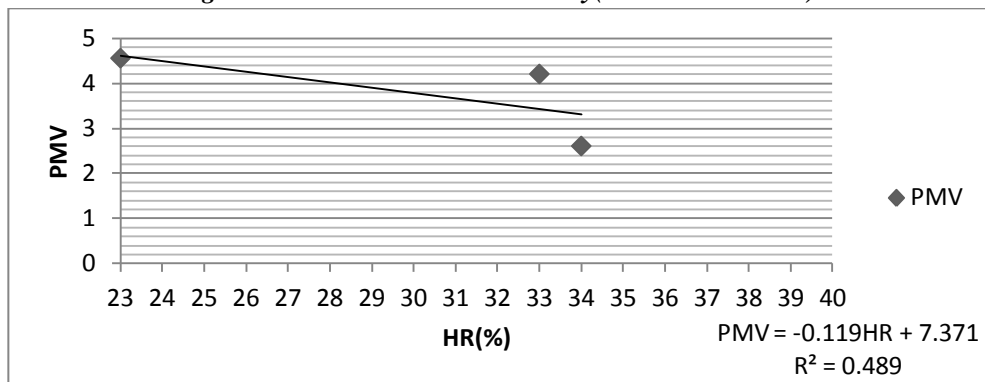


Figure 7-b : Neutral relative humidity(Plain area)

4.9. AMV and relative humidity

Figure 8 presents the relationship between the AMV and the relative humidity. Fig 8-a (mountain area) and Fig 8-b (plain), give us the following linear regression equations:

♦ Mountainous area

$$\text{PMV} = 0.108 \text{ HR} - 3.278 ; R^2 = 0.92 \quad (21)$$

$$\text{For AMV}=0, \text{ we have : HR}_{\text{neutral}} = 30.35 \% \quad (22)$$

♦ Plain area

$$\text{PMV} = 0.035 \text{ HR} - 1.821 ; R^2 = 0.184 \quad (23)$$

$$\text{For AMV}=0, \text{ we have : HR}_{\text{neutral}} = 52.02 \% \quad (24)$$

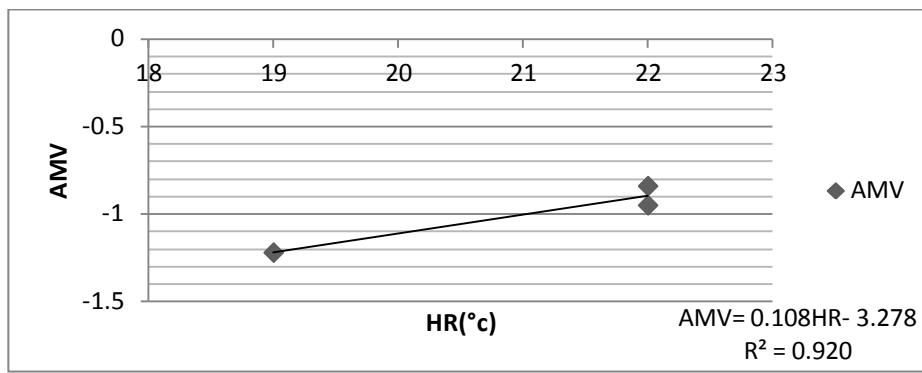


Figure 8-a :Neutral relative humidity(Mountainous area)

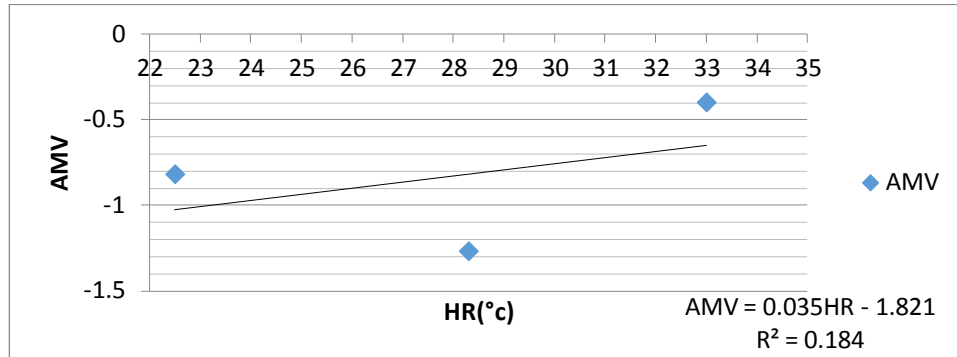


Figure 8-b :Neutral relative humidity(Plain area)

One could see that the neutral relative humidity of the mountain area with regard to public administrations, educational institutions and hotels, is not in adequacy with the directives for the internal climatic conditions (Christophe Zurcher-Thomas Franck) who recommend a relative humidity between 40 and 60% for offices and living rooms (Hotel), 45 and 55 % for Schools. While in the plain, it is in the above-mentioned intervals.

4.10. AMV and PMV

Figure 9 presents the relationship between de AMV and the PMV. Fig 9-a (mountain area) and Fig 10-b (plain), give us the following linear regression equations:

* Mountain area

$$PMV = -1.078AMV + 3.737 ; R^2 = 0.336 \quad (25)$$

For AMV=0, we have : PMV=3.737

* Plain area

$$PMV = -1.113AMV + 2.473; R^2 = 0.434 \quad (27)$$

For AMV=0, we have : PMV=2.473

In the mountains, we note that the PMV overestimates the thermal sensation in the case of our study, because for an AMV = 0 (neutral), the PMV = 3.737 (extremely hot). In the plain, we note that the PMV overestimates the thermal sensation in the case of our study, because for an AMV = 0 (neutral), the PMV = 2.473 (hot).

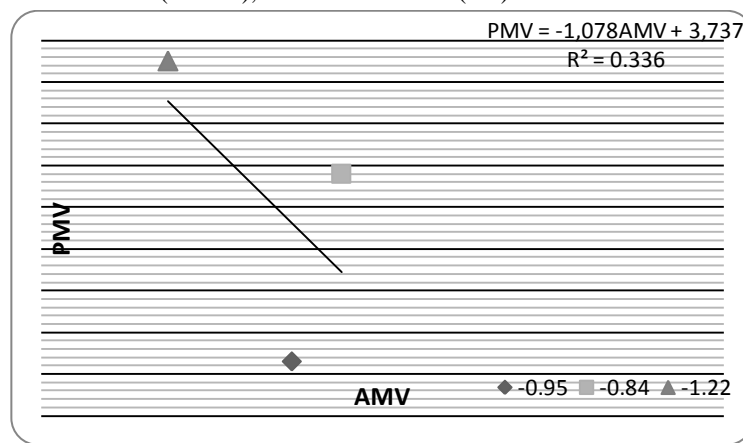


Fig 9-a: PMV-AMV (mountain area)

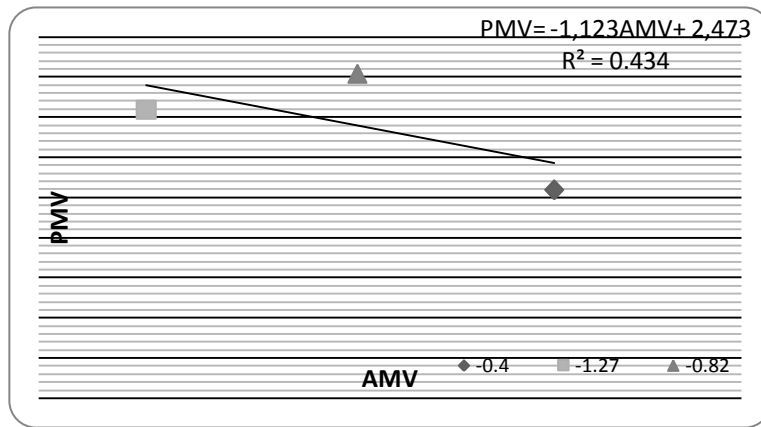


Fig 9-b: PMV-AMV (plain area)

4.11 Comfort zone

To obtain a thermal comfort situation, it is recommended that the PPD should be less than 5 %, which corresponds to a PMV between -0.5 and +0.5.

- ♦ *Mountain area*

$$AMV = -0.085Top + 1.708 ; R^2 = 0.458 \quad (29)$$

$$\text{For } AMV = -0.5, \text{ we have : } Top_1 = 22.45^\circ\text{C} \quad (30)$$

$$\text{For } AMV = 0.5, \text{ we have: } Top_2 = 14.20^\circ\text{C} \quad (31)$$

The operative temperatures of the comfort zone in the mountain zone are between 14.20°C and 22.45°C .

- ♦ *Plain area*

$$AMV = -0.148Top + 3.097 ; R^2 = 0.811 \quad (32)$$

$$\text{For } AMV = -0.5, \text{ we have : } Top_1 = 24.3^\circ\text{C} \quad (33)$$

$$\text{For } AMV = 0.5, \text{ we have : } Top_2 = 17.5^\circ\text{C}.$$

The operating temperatures of the comfort zone in the plain zone are between 17.5°C and 24.3°C .

5. Conclusion

The objective of this paper was to study thermal comfort in public buildings in the Sudano-Sahelian zone of Cameroon. In-situ data were taken during the harmattan season and the results based on the Actual Mean Vote showed that the neutral operative temperature varies between 20.09°C and 20.92°C while the neutral relative humidity was between 30.35 % and 61.94 % respectively for the mountain and plain areas. The operative temperatures of the comfort zone in the mountain area are between 14.20°C and 22.45°C while those of the plain area are between 17.5°C and 24.3°C . It was also observed that the thermal sensation is in the cold zone (slightly cold, cold and very cold) and that the PMV overestimates the thermal sensation. The occupants preferred the "neutral" thermal sensation (neither hot nor cold). The occupants have testified to "thermal unacceptable" especially for public administrations and schools. This is to say that the majority aspire for optimal thermal comfort.

6. Declaration of competing interest

The authors declare that there is no conflict of interest in regard with this work.

7. REFERENCES

- [1]- Benharkat S., Djamila RS. Approche adaptative du confort thermique dans les espaces d'enseignement universitaire à Constantine (Algérie). Sciences fondamentales et Engineering N°14/Janvier 2016. Pages 19 à 28.
- [2]- Djongyang N., Tchinda R., Njomo D. Thermal comfort: a review paper. Renewable and Sustainable Energy Reviews 14 (2010a): 2626-2640.
- [3]- Roumaissa A., Noureddine Z, Djamila D., Moussadek B. Etude expérimentale du comportement thermique des établissements scolaires dans les régions chaudes et arides. Courrier du Savoir-N°26, Mars 2018, pp259-268.
- [4]- Jannot Y., Djiaiko T. Economie d'énergie et confort thermique dans l'habitat en zone tropicale. Rev.Int.Froid 1994 Volume 17 Numéro 3.
- [5]- Bouthaina B. Evaluation du confort thermique et son impact sur l'habitat collectif. Mémoire de fin d'études, Université El Arabi Ben ,2016.
- [6]- Ioannou A., Itard L.. In-situ and real time measurements of thermal comfort and its determinants in thirty residential dwellings in the Netherlands. Energy and Buildings 139 (2017) 487-505.

- [7]- Castaño-Rosa R., Rodríguez-Jiménez CE., Rubio-Bellido C.R. Adaptive thermal Comfort Potential in Mediterranean Office Buildings: A case Study of Torre Sevilla. *Sustainability* 2018,10,3091.
- [8]- Rijal H.B. et al.: Adaptive model and the adaptive mechanisms for thermal comfort in Japanese dwellings. *Energy and Buildings* (2019).
- [9]- Kemajou A., Mba L.. Matériaux de construction et confort thermique en zone chaude ; Applications au cas des régions climatiques camerounaises. *Revue Energies Renouvelables* Vol.14 N°2 (2011) 239-248
- [10]- Djongyang N., René Tchinda. An investigation into thermal comfort and residential thermal environment in an intertropical sub-saharan Africa region : Field study report during the Harmattan season in Cameroon. *Energy Conversion and Management* 51(2010b)1391-1397.
- [11]- ASHRAE, American Society of Heating Refrigerating and Air-conditionning Engineers,éd 2009.
- [12]- Fergus J., Susan R. Rethinking thermal comfort. *Building Research and Information*,45 :7,711-716.
- [13]- Berghout B., Forgues D., Monfet D. Simulation du confort thermique intérieur pour l'orientation d'un batiment collectif à Biskra,Algérie. Ecole de Technologie Supérieure,Montréal,Québec.
- [14]- Burrati C., Riccardi P. Adaptive analysis of thermal comfort in university classrooms :correlation between experimental data and mathematical models. *Build environ* 2009 ;44 :674-84.
- [15]- Cognati SP, Ansaldi R, Filippi M. Thermal comfort in Italian classrooms under free running conditions during mid-seasons :assessment through objective and subjective approaches .*Building and Environment* 2009 ;44 :785-92.
- [16]- Heschong L. *Architecture et volupté thermique*. Parentheses. Marseille: p.93
- [17]- Hwang RL, Lin TP ,Cheng MJ, Chien JH. Patient thermal comfort requierement for hospital environments in Taiwan. *Building and Environment* 2001 ;36 :711-20.
- [18]- Izard. *Architecture d'été construite pour le confort d'été*. Aix-en-Provence : Edisud,141 p .1034-1049.
- [19]- Martin O. *L'analyse quantitative des données*. 4é édition. Erman Colin.
- [20]- Mokhtari AM, Brahimi K., Benziada R. *Architecture et confort thermique dans les zones arides –Application au cas de la ville de Béchar*. *Revue Energies Renouvelables* Vol.11 N°2 (2008) 307-315.
- [21]- Pigg S., Eilers M., Reed J . Behavioral aspects of lighting and occupancy sensors in private offices ;a case study of a university office building. ACEEE Summer Study on Energy Efficiency in Buildings.p 8161-8171.



Revue des Matériaux & Energies Renouvelable

Journal home : www.cu-relizane.dz

ISSN : 2507-7554

E- ISSN : 2661-7595



Simulation et optimisation de l'épaisseur de l'émetteur d'une cellule solaire mono-jonction à base de GaAs

Open
Access

H.Charane^{1,*}, A.Mahrane², A.Mesrane³ et H.Mazouz⁴

¹Laboratoire de Traitement de Surface et de Matériaux (LTSM), Département de Mécanique, Faculté de technologie Université de Blida (USDB 1), Route de Soumaa, BP 270, Blida, 09000 Blida

²Unité de Développement des Equipements Solaires, UDES/Centre de Développement des Energies Renouvelables (CDER), Route Nle n°11, BP386, 42415, Bou Ismail, Algeria

³Département Matériels et Équipements Intendance, Centre de Recherche-Développement de l'Intendance (CRD-INT), 09000 Blida, Algérie

⁴Département des Energies Renouvelables, Faculté de Technologie, Université de Blida (USDB 1), Route de Soumaa, BP 270, Blida, 09000 Blida

RESUME

Ce travail consiste en la simulation et l'optimisation de l'épaisseur de l'émetteur de type N d'une cellule solaire mono-jonction à base de GaAs à l'aide de l'outil de simulation Silvaco TCAD. L'objectif principal de cette étude est l'amélioration du rendement des cellules solaires mono-jonction GaAs. Les propriétés physiques, optiques et électriques du matériau GaAs ainsi que les différents phénomènes physiques pouvant avoir lieu dans la structure de la cellule solaire GaAs ont été tenus en considération lors des simulations. La structure optimale de la cellule solaire mono-jonction GaAs obtenue présente, dans les conditions de fonctionnement standard (AM 1.5, 1000W/m² et 300K), un rendement élevé de 28.56%. Par ailleurs, l'effet de la variation de l'épaisseur de l'émetteur sur les paramètres électriques de la cellule solaire a aussi été étudié.

Article history:

Received march 22, 2020

Received in revised form ...31 march 2020...

Accepted 09 July 2020

Keys word: cellule solaire mono-jonction, GaAs, épaisseur de l'émetteur, rendement .

Copyright © 2020 - All rights reserved

1. Introduction

Les semi-conducteurs III-V sont considérés comme les matériaux les plus adaptés pour la fabrication des cellules solaires à haut rendement en raison de leurs propriétés attractives pour le photovoltaïque notamment une large plage de couverture du spectre solaire [1], ainsi qu'une excellente résistance aux radiations solaires et aux températures élevées [2].

Il est à noter que pour les cellules solaires mono-jonction, la valeur optimale de l'énergie de gap la plus adaptée au spectre solaire AM1.5G est 1.39eV [3,4]. Le matériau ayant l'énergie de gap la plus proche de cet optimum est l'arsénure de gallium GaAs (1.42eV) qui est un semi-conducteur III-V à gap direct, composé de deux semi-conducteurs de la colonne III et V. L'arsénure de gallium (GaAs) est un matériau attrayant pour le photovoltaïque grâce à son fort coefficient d'absorption lui permettant de réaliser des cellules solaires ultra-minces pouvant absorber jusqu'à 90% des photons incidents dans une épaisseur de 3µm [5], une forte mobilité des électrons [6-7], une forte résistance aux radiations solaire et une bonne stabilité face aux températures élevées. De plus, la possibilité de transformer facilement l'arsénure de gallium en un semi-conducteur ternaire [7], a favorisé aussi son utilisation dans les cellules solaires multi-jonctions.

Depuis plusieurs années, les cellules solaires à base du GaAs suscitent l'intérêt des chercheurs et cela s'est traduit par de nombreux travaux de recherche [8-12]. En 1979, J.C.C. Fan et al. [8] ont fabriqué une cellule mono-jonction à base du GaAs sur un substrat de Germanium (Ge), présentant un rendement de 21%. En 2009, G.J. Bauhuis et al. [9] ont conçu une cellule solaire mono-jonction à base de GaAs pouvant présenter un rendement de 26.1%. La cellule solaire GaAs réalisée par Lin et al. [10] a pu atteindre un rendement de 18.9% en utilisant des puits quantiques à base de CdS.

* hamidcharane@gmail.com

En 2013, M. Abderrezek et al. [11] ont caractérisé et optimisé une cellule solaire mono-jonction GaAs en utilisant le logiciel PC1D, pouvant présenter un rendement de 25.8%. Récemment, la cellule solaire à triple-jonction à base de GaInP/GaAs/Ge simulée par J.W. Leem et al. [12] en utilisant le logiciel TCAD-Silvaco, a présenté un rendement de 30.72%.

Dans l'optique de concevoir une cellule solaire multi-jonction pour application terrestre, nous nous sommes d'abord intéressés à étudier à l'aide de l'outil de simulation TCAD-Silvaco une cellule solaire mono-jonction à base du matériau GaAs. L'objectif de ce travail est d'optimiser l'épaisseur de l'émetteur de la cellule solaire mono-jonction à base de GaAs afin d'atteindre un rendement maximal et d'en minimiser le coût de fabrication. Lors de ce travail, l'effet de la variation de l'épaisseur de l'émetteur sur les paramètres électriques de la cellule solaire sera aussi étudié.

II. Modélisation Et Simulation

II.1. Modélisation électrique de la cellule solaire photovoltaïque

Le schéma électrique équivalent d'une cellule solaire photovoltaïque, représentée par la figure 1, comporte une source de courant, une diode montée en parallèle, une résistance série R_s et une résistance parallèle R_p pour modéliser respectivement, les pertes ohmiques et les courants de fuite dus aux recombinaisons [13].

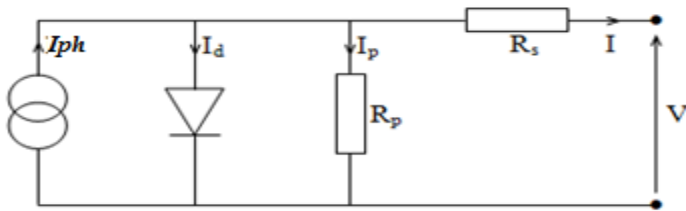


Figure 1– Schéma équivalent d'une cellule solaire photovoltaïque

Le courant délivré par une cellule solaire photovoltaïque est donné par [13] :

$$I = I_{ph} - I_s \left[\exp\left(\frac{qV}{nKT}\right) - 1 \right] - \frac{V}{R_p} \quad (1)$$

Où I_{ph} est le courant photo-généré, I_s le courant de saturation, V la tension aux bornes de la cellule solaire et n le facteur d'idéalité de la diode, K la constante de Planck et T la température.

Les cellules solaires photovoltaïques sont caractérisées principalement par cinq paramètres électriques : le courant électrique de court-circuit, la tension de circuit ouvert, la puissance maximale débitée, le facteur de forme et le rendement de conversion photovoltaïque.

Le courant de court-circuit est obtenu lorsque la tension aux bornes de la cellule solaire est nulle [14] :

$$V = 0 \Rightarrow I_{cc} = I_{ph} \quad (2)$$

La Tension de circuit-ouvert (V_{oc}) est obtenue aux bornes de la cellule solaire lorsque le courant électrique est nul comme suit [14] :

$$I = 0 \Rightarrow V_{oc} = \frac{KT}{q} \ln \left(\frac{I_{cc}}{I_{cc} + \frac{V_{oc}}{R_s}} \right) \quad (3)$$

Le Facteur de forme (FF) représente l'idéalité électrique de la cellule solaire et il est donné par [14] :

$$FF = \frac{P_{max}}{I_{cc}V_{oc}} = \frac{I_{max}V_{max}}{I_{cc}V_{oc}} \quad (4)$$

Où I_{max} et V_{max} sont respectivement le courant et la tension correspondant la puissance maximale (P_{max}) de la cellule solaire.

Le Rendement de conversion photovoltaïque (η) est donné par [14] :

$$\eta = \frac{P_{max}}{P_{in}A} = \frac{FFI_{cc}V_{oc}}{P_{in}A} \quad (5)$$

Où P_{in} puissance incidente et A surface de la cellule solaire.

II.2. Structure de la cellule solaire GaAs

La structure initiale de la cellule solaire GaAs étudiée est constituée d'une région émetteur de $1\mu\text{m}$ d'épaisseur avec une concentration de dopage de type N de $4 \times 10^{17} \text{ cm}^{-3}$ et d'une région base d'une épaisseur de $9.6\mu\text{m}$ avec une concentration de dopage de type P de $7 \times 10^{18} \text{ cm}^{-3}$.

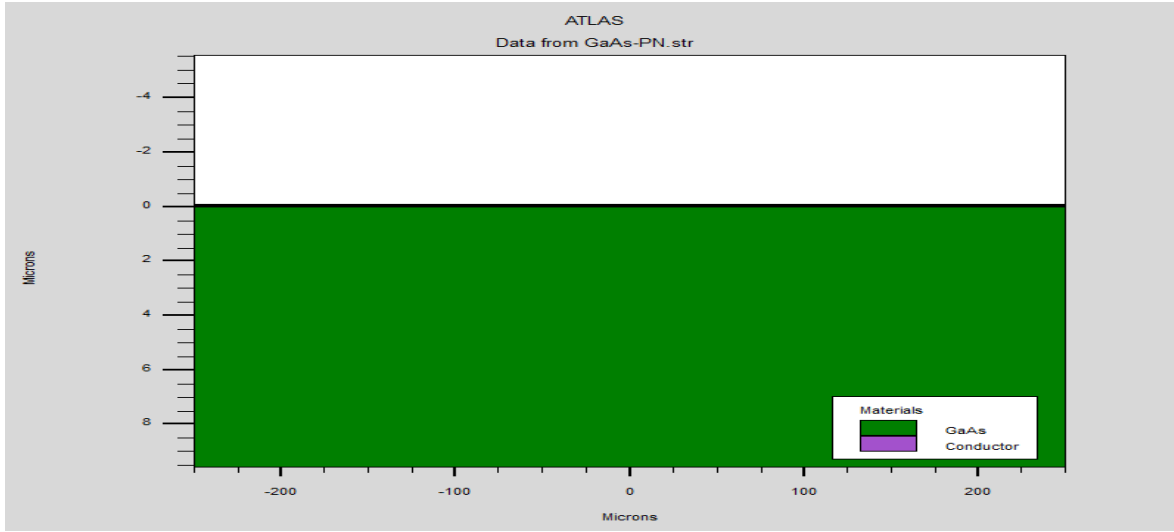


Figure 2– Schéma de la structure de la cellule solaire à base de GaAs sous TCAD

Lors de cette étude et afin de simplifier les simulations, nous avons supposé que les réflexions de la lumière de la face avant sont négligeables. De plus, afin de prendre en considération les différents phénomènes physiques pouvant avoir lieu dans la structure de la cellule solaire GaAs, nous avons implémenté et utilisé lors des simulations, les modèles physiques suivants :

- Modèle de la recombinaison Auger.
- Modèle de recombinaison Schokly-Read-Hall.
- Modèle de recombinaison radiative.

L'ensemble des simulations de la cellule solaire GaAs ont été effectuées dans les conditions de fonctionnement standards (AM1.5, 0.1W/cm^2 et 300K).

Les propriétés de l'alliage GaAs utilisées lors des simulations sont résumées dans le tableau ci-dessous.

Tableau 1. Les propriétés électriques et cristallines du matériau GaAs

Paramètre	GaAs	Réf.
Energie de gap Eg(eV)	1.424	[15]
Affinité électronique (eV)	4.07	[15]
Constante de maille (\AA°)	5.6533	[15]
Permittivité électrique	12.9	[15]
Densité effective d'états Nc (cm^{-3})	4.7×10^{17}	[15]
Densité effective d'états Nv (cm^{-3})	9.8×10^{18}	[15]
Concentration des porteurs intrinsèque	2.1×10^6	[15]
Masse effective des électrons $\frac{m_e^*}{m_0}$	0.067	[15]
Masse effective des trous $\frac{m_h^*}{m_0}$	0.642	[15]

III. Résultats Et Discussions

III.1. Optimisation de l'épaisseur de l'émetteur (Type N)

Afin de trouver l'épaisseur optimale de l'émetteur type N, nous avons simulé la cellule solaire mono-jonction GaAs pour différentes épaisseurs de l'émetteur allant de $0.001\mu\text{m}$ jusqu'à $1\mu\text{m}$. Pour chacune des valeurs de l'épaisseur de l'émetteur, les paramètres électriques de la cellule solaire ont été déterminés, comme illustrés dans les figures (3-5). Comme le montre la figure 3, la tension de circuit ouvert augmente avec l'augmentation de l'épaisseur de l'émetteur, alors que la densité de courant de court-circuit augmente d'abord, puis diminue. La cellule solaire GaAs délivre une densité de courant de court-circuit maximale de 37.23 A/cm^2 pour une épaisseur de l'émetteur de $0.003\mu\text{m}$.

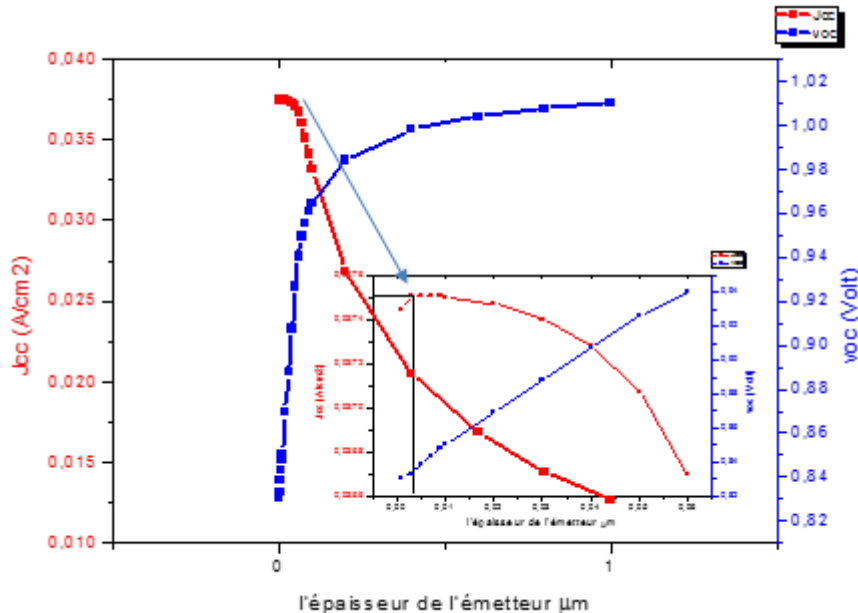


Figure 3—Densité de courant de court-circuit et la tension de circuit ouvert en fonction de l'épaisseur de l'émetteur pour une cellule solaire GaAs N/P.

La figure 4 montre que lorsque l'épaisseur de l'émetteur augmente, la puissance maximale produite par la cellule solaire GaAs augmente d'abord, puis diminue. La cellule solaire GaAs produit une puissance électrique maximale lorsque l'épaisseur de l'émetteur est $0.05\mu\text{m}$.

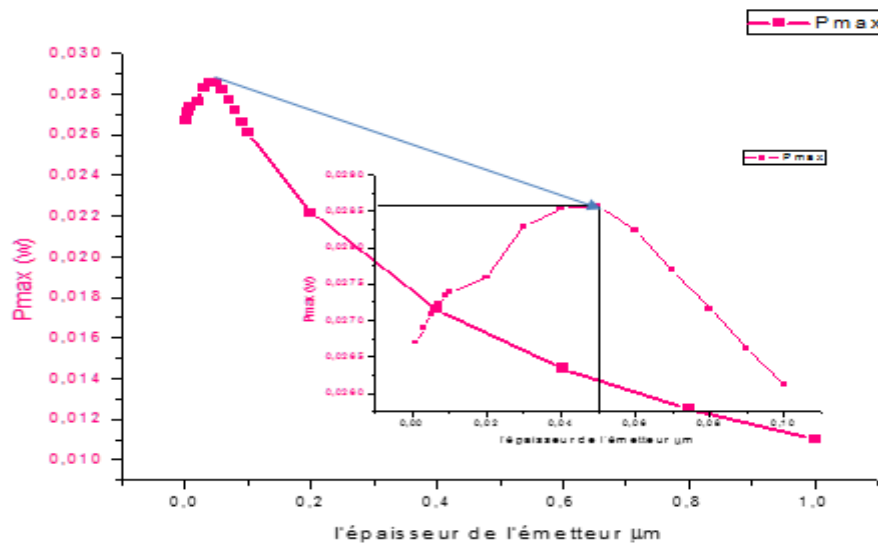


Figure 4—Puissance électrique P_{max} en fonction de l'épaisseur de l'émetteur pour une cellule GaAs N/P.

D'après la figure 5, le rendement de conversion photovoltaïque de la cellule solaire GaAs augmente d'abord avec l'augmentation de l'épaisseur de l'émetteur, puis il diminue. La cellule solaire GaAs présente un rendement maximal de 28.56% lorsque l'épaisseur de l'émetteur est $0.05\mu\text{m}$.

Ainsi, l'épaisseur optimale de l'émetteur de la cellule solaire mono-jonction GaAs est de $0.05\mu\text{m}$.

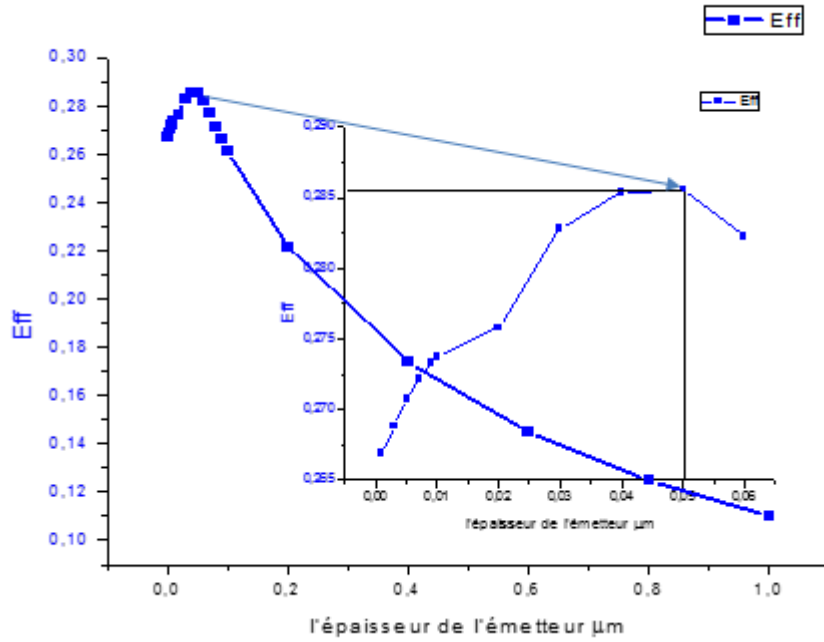


Figure 5– Le rendement de la conversion en fonction de l'épaisseur de l'émetteur

III.2. Caractéristiques électriques de la cellule solaire GaAs

Les caractéristiques électriques de la structure optimale de la cellule solaire GaAs sont données dans la figure 6. Elle présente dans les conditions de fonctionnement standards (AM1.5, 0.1W/cm² et 300K), les paramètres électriques suivants : $J_{cc}=37.23\text{mA/cm}^2$.

$$V_{oc}=0.93\text{V}.$$

$$P_{max}=28.57\text{mW}.$$

$$FF=82.56\text{ \%}.$$

$$\eta=28.56\text{ \%}.$$

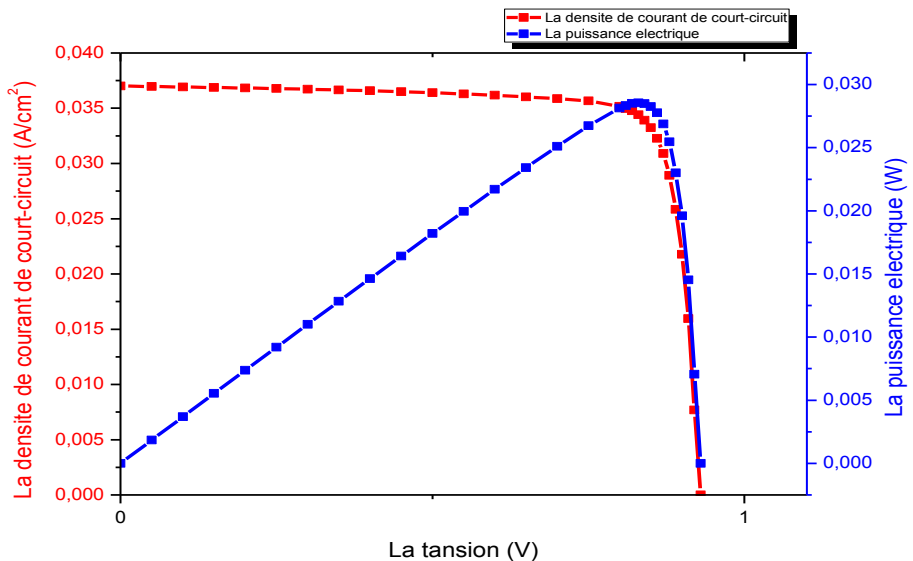


Figure 6– Caractéristiques électriques I(V) et P(V) de la cellule solaire GaAs optimale

La comparaison de nos résultats avec ceux obtenus et publiés auparavant par M. Kayes et al. [16], montre que le rendement de la cellule solaire GaAs que nous proposons, a un meilleur rendement 28.56% contre 27.6% [16]. La cellule solaire optimale GaAs que nous avons; conçue nous a permis d'améliorer le courant de court-circuit d'une cellule solaire GaAs à une jonction.

IV. Conclusion

Lors de cette étude, nous avons optimisé l'épaisseur de l'émetteur d'une cellule solaire GaAs mono-jonction afin d'améliorer le rendement de conversion photovoltaïque. Pour cela, la cellule solaire GaAs a été simulée en utilisant TCAD-Silvaco pour différentes épaisseurs de l'émetteur.

Les résultats obtenus montrent que lorsque l'épaisseur de l'émetteur augmente, les paramètres électriques de la cellule solaire GaAs augmentent d'abord, puis diminuent. La cellule solaire mono-jonction GaAs présente dans les conditions de fonctionnement standards un rendement maximal de 28.56% pour une épaisseur optimale de l'émetteur de $0.05\mu\text{m}$.

La comparaison de nos résultats avec ceux publiés auparavant montre que la cellule solaire que nous proposons présente un meilleur rendement.

REFERENCES

- [1] Dimroth. F and Kurtz. S, March 2007, "Hight-Efficiency Multijonction Solar Cells", MRS bulletin, Vol. 32, www.mrs.org/bulletin.
- [2] Evoy. A. Mc, Markvart. T and Castaner. L, 2012, "Practical Handbook of Photovoltaics Fundamentals and Applications", Second Edition, Elsevier Ltd, ISBN: 978-0-12- 3859334-1.
- [3] Zdanowicz. T, Rodziewicz. T, Zabkowska-Waclawek. M, May 2005, "Theoretical analysis of the optimum energy band gap of semiconductors for fabrication of solar cells for applications in higher latitudes locations", Solar Energy Materials and Solar Cells, vol.87, pp 757-769.
- [4] Mesrane. A, Mahrane. A, Rahmoune. F., and Oulebsir. A, 2017, "Optimal band gaps for InGaN single and double junction solar cells", in Proceedings of the International Conference on Advanced Systems and Electrical Technologies (IC_ASET).
- [5] Green. M, 1998, "Solar Cells, Operating Principles, Technology and System Applications", University of New South Wales.
- [6] Brozel. MR and Stillman. GE, 1996, "Properties fo Gallium Arsenides", 3rd edition, Institution of Electrical Engineers.
- [7] Jha. A. R, 2010, "Solar cell Technology and applications", Taylor & Francis Group, p.26, ISBN 978-1-4200-8177-0.
- [8] Fan. John C. C, Bozler Carl O, and Palm Barbara J, 1 December 1979, "Calculated and measured efficiencies of thinfilm shallowhomojunction GaAs solar cells on Ge substrates", Appl. Phys. Lett. 35(11).
- [9] Bauhuis. G.J, Mulder. P, Haverkamp. E.J, Huijben. J.C.C.M and Schermer. J.J, 2009, "26.1% thin-film GaAs solar cell using epitaxial lift-off", Solar Energy Materials & Solar Cells, doi:10.1016/j.solmat.2009.03.027
- [10] Lin. C.C, Chen. H.C, Tsai. Y.L, Han. H.V, Shih. H.S, Chang. Y.A, Kuo. H.C, and Yu. P, 2012, "Highly efficient CdS-quantum-dot-sensitized GaAs solar cells", Optical Society of America, Vol. 20, No. S2 / OPTICS EXPRESS A319.
- [11] Abderrezek. M, Djahli. F, Fathi. M and Ayad. M, 2013, "Numerical Modeling of GaAs Solar Cell Performances, ELEKTRONIKA IR ELEKTROTECHNIKA, ISSN 1392-1215, VOL. 19, NO. 8, <http://dx.doi.org/10.5755/j01.eee.19.8.5392>.
- [12] Leem. J.W and Yu. J.S, May 2014, "Theoretical Modeling and Optimization of III-V GaInP/GaAs/Ge Monolithic Triple-junction Solar Cells", Journal of the Korean Physical Society, Vol. 64, No. 10, pp. 1561~1565.
- [13] Bonkoungou. D, Koalaga. Z and Njomo. D, March 2013, "Modelling and Simulation of photovoltaic module considering single-diode equivalent circuit model in MATLAB", International Journal of Emerging Technology and Advanced Engineering, Volume 3, Issue 3).
- [14] Li. Z, Xiao. H, Wang. X, Wang. C, Deng. Q, Jing. L, Ding. J, and Hou. X, 2013, "Theoretical simulations of InGaN/Si mechanically stacked two-junction solar cell", Physica B: Condensed Matter, vol. 414, pp. 110–114. Doi: 10.1016/j.physb.2013.01.026.
- [15] Levinstein. M, Rumyantsev. S and Shur. M, 1999, "HANDBOOK SERIES ON SEMICONDUCTOR PARAMETERS", VOLUME 2: Ternary and Quaternary A3BJ Semiconductors, World Scientific, Singapore, New Jersey London, Hong Kong.
- [16] Kayes. B.M, Nie. H, Twist. R, Spruytte. S.G, Reinhardt. F, Kizilyalli. I.C, and Higashi. G.S, 2011, "27.6% CONVERSION EFFICIENCY, A NEW RECORD FOR SINGLE-JUNCTION SOLAR CELLS UNDER 1 SUN ILLUMINATION", IEEE.



Revue des Matériaux & Energies Renouvelable

Journal home : www.cu-relizane.dz

ISSN : 2507-7554

E- ISSN : 2661-7595



Une nouvelle théorie quasi-3D de déformation de cisaillement pour l'analyse statique des poutres stratifiées à couches croisées symétriques et antisymétriques en matériaux non homogènes

Open Access

KADDARI Miloud^{1,*}, KAÇI Abdelhakim^{1,2}, TOUNSI Abdelouahed¹

¹ Laboratoire des Matériaux et Hydrologie, Département de Génie Civil et Travaux Publics, Université Djilali Liabes de Sidi Bel-Abbes, Faculté de technologies, BP 89 Cité Ben M'hidi 22000 Sidi Bel-Abbes, Algérie.

² Université Dr Tahar Moulay, Faculté de Technologie, Département de Génie Civil et Hydraulique, BP 138 Cité En-Nasr 20000 Saida, Algérie.

RESUME

Article history:

Received: July 23, 2020

Received in revised form July 25, 2020

Accepted August 18, 2020

Keys word: Static flexure; laminated beams ; symmetric and anti-symmetric ; cross-ply.

Dans cette recherche, une théorie de déformation de cisaillement trigonométrique prenant en compte de l'effet de déformation de cisaillement transversal ainsi que l'effet d'étirement est présentée pour l'analyse de la flexion statique des poutres stratifiées à couches croisées symétriques et antisymétriques. Le champ de déplacement utilise une fonction sinusoïdale en termes de coordonnée d'épaisseur pour inclure l'effet de déformation par cisaillement transversal. La fonction cosinus en coordonnées d'épaisseur est utilisée dans le déplacement transversal pour inclure l'effet de la déformation normale. Il prend en compte de la variation réaliste de la contrainte de cisaillement transverse à travers l'épaisseur et satisfait les conditions de nullités des contraintes de cisaillement au niveau de la surface supérieure et inférieure de la poutre. La théorie élimine le besoin de facteur de correction de cisaillement. Les équations et les conditions aux limites de la théorie sont obtenues en utilisant le principe des travaux virtuels. Des résultats sont obtenus pour la flexion statique des poutres stratifiées à couches croisées symétriques et antisymétriques. Ces résultats sont comparés à ceux d'autres théories modifiées et la solution d'élasticité disponible dans la littérature scientifique.

Copyright © 2020 - All rights reserved

1. Introduction

Dans les poutres composites stratifiées, la déformation transversale par cisaillement affecte de manière significative le déplacement transversal, les fréquences propres de vibration et les charges de flambement. La théorie élémentaire des poutres (TEB), qui repose sur l'hypothèse d'Euler-Bernoulli selon laquelle les plans initialement normaux au plan médian restent plans et perpendiculaires à la surface moyenne après flexion, conduit à des pourcentages d'erreur élevés dans l'analyse des poutres anisotropes en raison de la négligence des déformations du cisaillement transversal.

La théorie de la déformation par cisaillement du premier ordre (FSDT) est une amélioration par rapport à la théorie élémentaire de la poutre Reissner [3]; Mindlin [17]; Reissner [2]. Cette théorie est cependant appelée théorie de Timoshenko dans les poutres. Dans la théorie de Timoshenko, la répartition de la contrainte de cisaillement transverse est constante à

* Corresponding author. E-mail address: kaddari_mil@yahoo.fr

travers toute l'épaisseur de la poutre et exige un facteur de correction de cisaillement pour corriger l'énergie de contrainte de la déformation Thai and Vo [22]; Thai and Vo [23].

Les limitations de la théorie élémentaire des poutres (TEB) et de la théorie de la déformation par cisaillement du premier ordre (FSDT) ont imposé le développement de théories de la déformation par cisaillement d'ordre supérieur (HSDT). La théorie d'ordre élevée (HSDT) donne une représentation correcte de la contrainte de cisaillement.

Par la suite, différentes théories d'ordre supérieur plus précises que les modèles du premier ordre ont été proposées par Levinson [9], Ambartsumian [1], Touratier [24], Soldatos [21], Karama et al. [7] and Reddy [18] afin de satisfaire les conditions aux limites sur les bords libres de la poutre.

Lo, Christensen et Wutheory [10, 11] ont développé une théorie cohérente d'ordres élevés pour les plaques homogènes et stratifiées, comprenant les effets de la déformation en cisaillement transverse, de la déformation normale transversale et de la distribution non linéaire des déplacements par rapport à la coordonnée épaisseur. La théorie contient onze variables de déplacement. Cette théorie est largement utilisée par de nombreux chercheurs pour l'analyse des poutres et plaques déformables par cisaillement et les solutions sont obtenues par la méthode des éléments finis.

Khdeir et Reddy [8] ont présenté l'analyse des poutres stratifiées à couches croisées symétriques et antisymétriques à l'aide des théories classique de premier ordre, de deuxième ordre et de troisième ordre. Kant et Manjunatha [6] et Manjunatha et Kant [13, 14] ont développé un ensemble de théories d'ordre supérieur pour l'analyse des poutres composites et sandwich utilisant la théorie de Lo, Christensen et Wu [10, 11]. Maiti et Sinha [12] et Vinayak et al. [25] ont présenté l'analyse par éléments finis des poutres stratifiées épaisses symétriques et asymétriques basées sur la théorie d'ordres supérieurs de Lo et al. [10]. Soldatos et Elishakoff [20] ont développé une théorie de la déformation par cisaillement du troisième ordre pour l'analyse statique et dynamique d'une poutre orthotrope basée sur la théorie classique des poutres. La théorie intègre les effets du cisaillement transverse et de la déformation normale transversale.

Muskhelishvili [15] à effectué une analyse tridimensionnelle de l'élasticité de poutres non homogènes en flexion, toutes les couches ayant le même coefficient de Poisson. L'analyse se complique lorsque chaque couche à un coefficient de Poisson différent. Silverman [19] à présenté des solutions d'élasticité pour la flexion de poutres orthotropes sous des charges polynomiales en utilisant les fonctions de contrainte d'Airy. Des formules sont données pour les contraintes axiales de flexion, la flèche et le cisaillement transversal pour les poutres simplement appuyées et en porte-à-faux. Pagano [16] à présenté des solutions d'élasticité exacte pour les stratifiés composites en flexion cylindrique. Un stratifié unidirectionnel et des stratifiés à couches croisées à deux et trois couches soumis à une charge sinusoïdale sont considérés. Ghugal et Shimpi [4] ont présenté une revue récente de ces théories avec orientation nouvelle.

Dans ce travail, l'accent a été mis sur le développement d'une nouvelle théorie de déformation de cisaillement quasi-3D pour l'analyse statique des poutres stratifiées à couches croisées symétriques et antisymétriques tenant compte des effets de cisaillement transversal et l'effet d'étirement (déformation normale). Dans cette théorie raffinée, la composante du déplacement transversale \mathbf{w} peut être dissociée en deux termes: le premier \mathbf{w}_b représente une partie de la flèche pure de la poutre, tel que la dérivée de cette composante égale à la rotation de la section transversale, le second terme \mathbf{w}_s , représente la flèche induit par l'effet de la déformation de cisaillement de la section transversale. Les équations d'équilibre sont déterminées à partir du principe du travail virtuel. Des solutions analytiques de type Navier sont utilisées pour les poutres stratifiées à couches croisées pour des conditions aux limites simplement supportées. La performance du modèle proposé est vérifiée en comparant les résultats numériques avec des solutions d'élasticités et d'autres théories d'ordre élevé disponibles dans la littérature.

2. Formulations théoriques

2.1 Relations cinématiques et équations constitutives

Dans cette recherche, un champ de déplacement selon la théorie de déformation de cisaillement d'ordre élevé quasi-3D s'écrivent:

$$u(x, z) = u_0(x) + w_b(z) \frac{w_b}{x} f(z) \frac{w_s}{x} \quad (1.a)$$

$$w(x, z) = w_b(x) + v_s(x) g(z) \frac{w_s}{x} \quad (1.b)$$

Où u et w sont des déplacements dans les directions x et z , respectivement. u_0 est le déplacement du plan médian de la poutre ($x=0$). Un déplacement additionnel φ est introduit pour prendre en compte l'effet de la contrainte normal (l'effet d'étirement).

$f(z)$ et $g(z)$ sont des fonctions de formes avec :

$$f(z) = z \sin \frac{\pi z}{h} \quad \text{et} \quad g(z) = 1 - f(z) \quad (2.a)$$

$$\text{Où : } f(z) = \frac{df(z)}{dz} \quad (2.b)$$

Le champ des déformations se déduit du champ des déplacements des équations (1.a) et (1-b), soit :

$$\begin{aligned} \frac{\partial u}{\partial x} &= \frac{\partial}{\partial x} \left(u_0(x) + w_b(z) \frac{w_b}{x} f(z) \frac{w_s}{x} \right) \\ &= \frac{\partial w_b}{\partial x} f(z) \frac{w_s}{x} \\ &= g(z) \frac{\partial w_b}{\partial x} \\ \frac{\partial^2 u}{\partial x^2} &= g'(z) \frac{\partial w_b}{\partial x} \\ \frac{\partial^3 u}{\partial x^3} &= 0 \end{aligned} \quad (3)$$

Où :

$$\frac{\partial w_b}{\partial x} = k_x^b, \quad k_x^b = \sqrt{\frac{w_b}{x^2}}, \quad k_x^s = \sqrt{\frac{w_s}{x^2}}, \quad (4.a)$$

$$\frac{\partial w_s}{\partial x} = k_x^s, \quad k_x^s = \sqrt{\frac{w_s}{x^2}}, \quad (4.b)$$

Les relations contraintes-déformations constitutives de la $k^{\text{ème}}$ couche de la poutre stratifiée peuvent être exprimées dans les coordonnées globales (x, y, z) comme suit:

$$\begin{array}{ccccccccc} \sigma_x & \sigma_z & \tau_{xz} & C_{11} & C_{13} & 0 & \tau_{xx} & \tau_{zz} & \\ \sigma_z & \sigma_x & -\tau_{xz} & C_{31} & C_{33} & 0 & \tau_{zx} & \tau_{xz} & \\ \tau_{xz} & -\tau_{zx} & \sigma_x & C_{13} & C_{31} & 0 & \tau_{xz} & \tau_{zx} & \\ \hline & & & 0 & 0 & C_{55} & & & \end{array} \quad (5)$$

Où ($\sigma_x, \sigma_z, \tau_{xz}$) sont les contraintes et ($\frac{\partial u}{\partial x}, \frac{\partial u}{\partial z}, \frac{\partial^2 u}{\partial x^2}$) sont les composantes de la déformation de la couche dans les coordonnées globales, et les C_{ij} sont des constantes matérielles données par Jones [5].

2.2. Principe des travaux virtuels

En vue d'établir de façon systématique l'ensemble des équations d'équilibre, ainsi que les conditions aux limites de la poutre en composite stratifiée, le principe des travaux virtuels peut être énoncé sous la forme suivante :

$$\delta U - \delta V = 0 \quad (6)$$

Où: δU est la variation de l'énergie de déformation et δV est la variation du travail des charges externes appliquée à la poutre. La substitution des expressions énergétiques appropriées peut être déterminée :

$$\int_0^L \left[b/2 \frac{\partial u}{\partial x} \sigma_x + \frac{\partial u}{\partial z} \sigma_z - \frac{\partial^2 u}{\partial x^2} \tau_{xz} - \frac{\partial^2 u}{\partial z^2} \tau_{zx} - \frac{\partial^3 u}{\partial x^3} C_{11} - \frac{\partial^3 u}{\partial z^3} C_{33} \right] A dz - \int_0^L \left[\sigma_b w_b + \sigma_s w_s + \sigma_{st} w_{st} \right] dx = 0 \quad (7)$$

2.3 Solution exacte pour une poutre simplement appuyée

Pour le cas d'une poutre simplement appuyée sur les deux cotés, les conditions aux limites pour la présente théorie s'écrivent:

$$w_b \bullet w_s \bullet \frac{w_s}{\partial x} \bullet N_x \bullet M_x^b \bullet M_x^s \bullet 0 \quad \text{à} \quad x \bullet 0, L \quad (8)$$

A partir de la solution de Navier, on peut résoudre le problème du comportement élastique de la flexion des poutres. Elle peut alors être recherchée en écrivant les déplacements u_0 , w_b , w_s et ω sous forme de simple série de Fourier, satisfaisant les conditions aux limites.

$$\begin{array}{l} u_0 \\ w_b \\ w_s \\ \omega \end{array} = \sum_{n=1}^{\infty} \begin{array}{l} U_n \cos(\frac{n\pi}{L}x) \\ W_{bn} \sin(\frac{n\pi}{L}x) \\ W_{sn} \sin(\frac{n\pi}{L}x) \\ \omega_n \sin(\frac{n\pi}{L}x) \end{array} \quad (9.a)$$

Où :

$$\omega \bullet 0 \text{ à } L \quad (9.b)$$

U_n , W_{bn} , W_{sn} and ω_n sont des paramètres arbitraires représentent l'amplitude de chacun des termes dans les séries pour la solution de Navier, λ est une constante. On obtient l'opérateur suivant :

$$\begin{bmatrix} A_{11} & A_{12} & A_{13} & A_{14} \\ A_{21} & A_{22} & A_{23} & A_{24} \\ A_{31} & A_{32} & A_{33} & A_{34} \\ A_{41} & A_{42} & A_{43} & A_{44} \end{bmatrix} \begin{bmatrix} U_n \\ W_{bn} \\ W_{sn} \\ \omega_n \end{bmatrix} = \begin{bmatrix} 0 \\ 0 \\ 0 \\ 0 \end{bmatrix} \quad (10)$$

Où A_{ij} c'est une matrice symétrique donnée par :

$$\begin{bmatrix} A_{11} & A_{12} & A_{13} & A_{14} \\ A_{21} & A_{22} & A_{23} & A_{24} \\ A_{31} & A_{32} & A_{33} & A_{34} \\ A_{41} & A_{42} & A_{43} & A_{44} \end{bmatrix} = \begin{bmatrix} \frac{1}{2}E_1I_1 & -\frac{E_1I_1}{L} & 0 & 0 \\ -\frac{E_1I_1}{L} & \frac{2E_1I_1}{L^2} + \frac{R}{L} & 0 & 0 \\ 0 & 0 & \frac{2E_1I_1}{L^2} + \frac{R}{L} & 0 \\ 0 & 0 & 0 & \frac{2E_1I_1}{L^2} + \frac{R}{L} \end{bmatrix} \quad (11)$$

Avec:

$$\begin{aligned} a_{11} &= \frac{E_1I_1}{2} \\ a_{12} &= -\frac{E_1I_1}{L} \\ a_{13} &= 0 \\ a_{14} &= 0 \\ a_{22} &= \frac{2E_1I_1}{L^2} + \frac{R}{L} \\ a_{23} &= 0 \\ a_{24} &= 0 \\ a_{33} &= \frac{2E_1I_1}{L^2} + \frac{R}{L} \\ a_{34} &= 0 \\ a_{44} &= \frac{2E_1I_1}{L^2} + \frac{R}{L} \end{aligned} \quad (12)$$

Le chargement transversal $q(x)$ agissant suivant l'axe z est exprimé sous forme de simple série de Fourier :

$$q(x) = \sum_{n=1}^{\infty} q_n \sin(\frac{n\pi}{L}x) \quad (13)$$

Les coefficients q_n sont donnés pour certaines charges comme suit:

$$q_n = \frac{2}{L} \int_0^L q(x) \sin \frac{n\pi x}{L} dx \quad (14)$$

$\bullet \frac{q_0}{2}$ pour un chargement sinusoïdale distribué.
 $\bullet \frac{4q_0}{n\pi}$ pour un chargement uniformément répartie.

Où q_0 représente l'intensité de la charge sur la poutre.

3. Résultats numériques et discussion

Nous présentons les résultats de l'analyse du comportement en flexion menée sur une poutre composite stratifié en utilisant une nouvelle théorie raffinée de déformation de cisaillement d'ordre élevé avec l'effet de la déformation normale.

Certaines études de convergence sont données à titre d'exemples afin de démontrer l'exactitude de la méthode. Les résultats sont également donnés pour les poutres composites à trois couches symétrique à empilement croisé ($0^\circ/90^\circ/0^\circ$) et deux couches antisymétrique à empilement croisé ($0^\circ/90^\circ$) pour différentes propriétés du matériau et des rapports longueur épaisseur variables.

Les stratifiés sont censés avoir des épaisseurs égales et faites avec les mêmes matériaux orthotropes dont les propriétés sont:

$$\frac{E_1}{E_2} = 25, \quad \frac{E_3}{E_2} = 1, \quad \frac{G_{12}}{E_2} = \frac{G_{13}}{E_2} = 0.5, \quad \frac{G_{23}}{E_2} = 0.2 \quad \text{et} \quad \frac{v_1}{v_2} = \frac{v_3}{v_2} = 0.25$$

Les solutions de référence sont données sous forme adimensionnelle. Il s'agit respectivement du déplacement transversal et des contraintes normales et tangentielles :

$$\bar{u} = \frac{E_2 b}{q_0 h} u, \quad \bar{w} = \frac{100 E_2 h^3}{q_0 L^4} w, \quad \bar{\sigma}_x = \frac{b}{q_0} \sigma_x, \quad \bar{\tau}_{xy} = \frac{b}{q_0} \tau_{xy}, \quad S = L/h$$

Tableau 1 : déplacement axiale maximale adimensionnelle \bar{u} à $z = 0, z = h/2$, déplacement transversal \bar{w} à $z = L/2, z = 0$, contraintes normales $\bar{\sigma}_x$ à $z = L/2, z = h/2$ et $\bar{\tau}_{xy}$ tangentielles à $z = 0, z = 0$ pour une poutre en matériau composite stratifié à couches croisées simplement appuyée ($0^\circ/90^\circ$) soumise à un chargement sinusoïdale pour différents rapports d'élancement.

$S = L/h$	Théorie	\bar{u}	\bar{w}	$\bar{\sigma}_x$	$\bar{\tau}_{xy}$
4	Présente $\bullet \square \bullet 0$	1.7185	4.3959	33.8266	2.5185
	Présente $\bullet \square \square 0$	1.7175	4.3923	33.8158	2.5187
	Mantari et Canales (2016) $\bullet \square \square 0$	1.7178	4.3936	33.8205	2.5187
	Timoshenko	1.4212	4.7966	27.9049	1.8189
	Euler –Bernoulli	1.4212	2.6254	27.9049	0
	Elasticité	1.5288	4.7080	30.0190	2.7212
10	Présente $\bullet \square \bullet 0$	22.9180	2.9090	180.4490	6.4260
	Présente $\bullet \square \square 0$	23.1718	2.9429	181.8662	6.4179
	Mantari et Canales (2016) $\bullet \square \square 0$	23.1767	2.9433	181.7666	6.4154
	Timoshenko	22.2060	2.9728	174.4052	4.5473
	Euler –Bernoulli	22.2060	2.6254	174.4052	0
	Elasticité	22.4760	2.9611	176.5300	7.2678

On remarque que les résultats trouvés dans le tableau 1 par la présente méthode sont en bon accord avec ceux trouvés dans la littérature et particulièrement avec ceux de Mantari et Canales (2016) avec $\bullet \square \square 0$. Ce qui important de signaler est

que le fait de négliger l'effet d'étirement augmente les déplacements et la contrainte pour un rapport d'élancement S=4 et l'inverse est observé pour S=10 et ceci est dû à l'effet du cisaillement qui est important dans les poutres courtes.

Le tableau 1 montre clairement que pour la théorie des poutres classiques basées sur les hypothèses d'Euler-Bernoulli (ETB), la contrainte de cisaillement transverse est nulle.

Tableau 2: Déplacement axiale maximale adimensionnelle \bar{u} à $z = h/2$, déplacement transversal \bar{w} à $z = L/2$, contraintes normales τ_x à $z = L/2$, z et tangentielles à $z = 0$ pour une poutre en matériau composite stratifié à couches croisées simplement supportée ($0^\circ/90^\circ/0^\circ$) soumise à un chargement sinusoïdale pour différents rapports d'élancement.

$S \bullet L/h$	Théorie	\bar{u}	\bar{w}	τ_x	ϵ_z
4	Présente $\epsilon_z \neq 0$	0.8901	2.7242	17.5208	1.1615
	Présente $\epsilon_z = 0$	0.8899	2.7053	17.6145	1.1607
	Reddy [18]	0.8653	2.7000	16.9898	1.1094
	Timoshenko	0.5136	2.4107	10.0854	0.6366
	Euler –Bernoulli	0.5136	0.5109	10.0854	0
	Elasticité	0.9150	2.8870	17.8800	1.4250
10	Présente $\epsilon_z \neq 0$	8.9968	0.8815	70.8377	3.0475
	Présente $\epsilon_z = 0$	8.9974	0.8816	70.8379	3.0475
	Reddy [18]	8.9398	0.8751	70.2128	2.8839
	Timoshenko	8.0257	0.8149	63.0339	1.5915
	Euler –Bernoulli	8.0257	0.5109	63.0339	0
	Elasticité	9.1050	0.8800	71.300	4.2000

On remarque que les résultats trouvés dans le tableau 2 sont inférieures à ceux trouvés pour une poutre en matériau composite stratifié ($0^\circ/90^\circ$) et ce, est essentiellement dû à l'augmentation de la rigidité.

Les déplacements \bar{u} et \bar{w} obtenu par la présente théorie sont sous estimés par rapport à la solution exacte et la contraintes normales τ_x obtenu est sous estimé par rapport à la solution exacte.

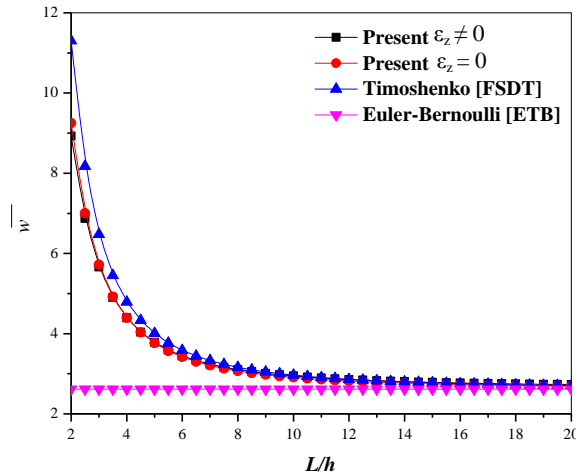


Figure 1: Variation du déplacement transverse \bar{w} de la poutre ($0^\circ/90^\circ$) soumise à un chargement sinusoïdale pour différents rapports d'élancement.

La figure 1 montrent la variation du déplacement transverse \bar{w} de la poutre ($0^\circ/90^\circ$) soumise à un chargement sinusoïdale pour différents rapport d'élancement L / h pour différentes théories. On voit que l'effet d'étirement $\epsilon_z \neq 0$ se fait sentir pour une poutre courte.

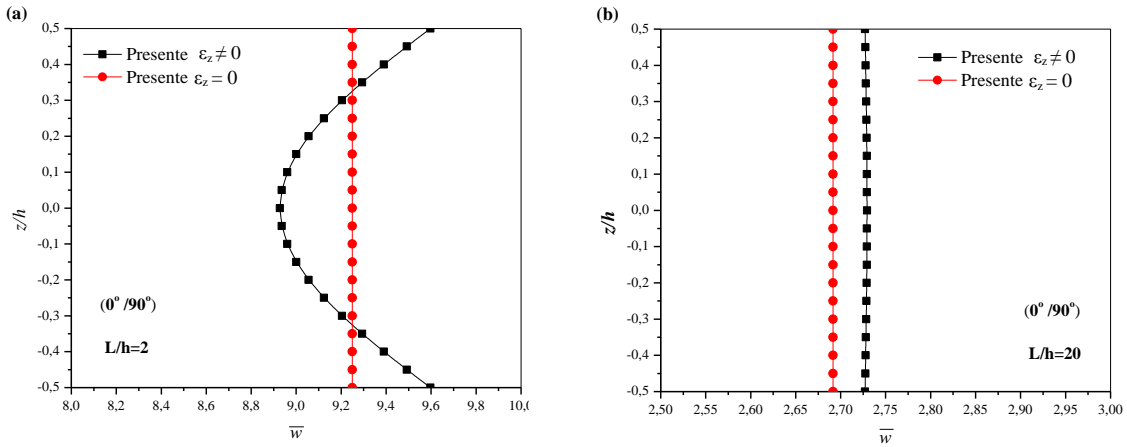


Figure 2: Variation du déplacement transverse \bar{w} de la poutre $(0^\circ/90^\circ)$ soumise à un chargement sinusoïdale à travers l'épaisseur de la poutre pour, (a) $L/h = 2$, (b) $L/h = 20$

La figure 2 montrent la variation du déplacement transverse \bar{w} de la poutre $(0^\circ/90^\circ)$ soumise à un chargement sinusoïdale à travers l'épaisseur de la poutre pour $L/h = 2$ et $L/h = 20$. On voit que l'effet d'étirement $\varepsilon_z \neq 0$ à une influence importante.

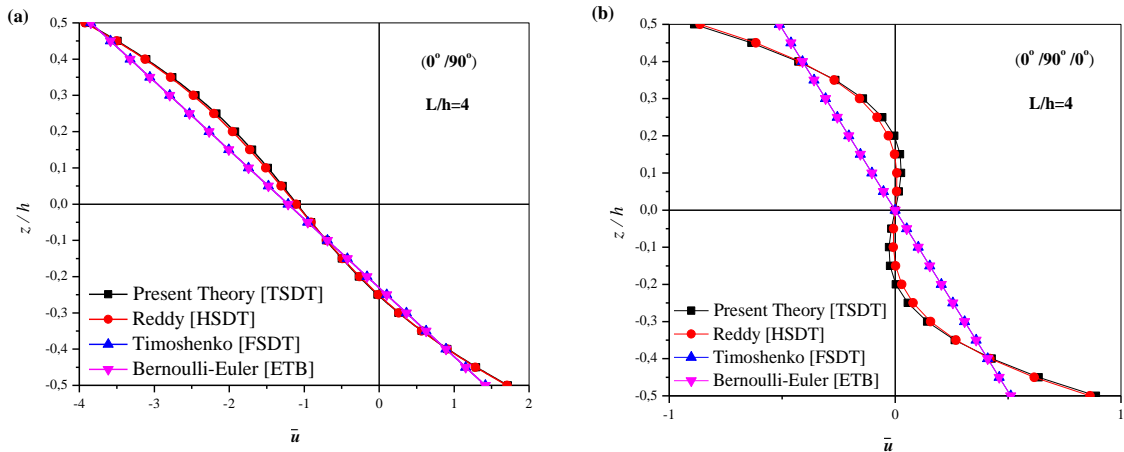


Figure 3: Variation du déplacement axial à travers l'épaisseur de la poutre soumise à un chargement sinusoïdale pour un rapport d'élancement de $L/h = 4$, (a). $(0^\circ/90^\circ)$, (b). $(0^\circ/90^\circ/0^\circ)$

La variation du déplacement axial adimensionnel à travers l'épaisseur de la poutre $(0^\circ/90^\circ)$ et $(0^\circ/90^\circ/0^\circ)$ soumise à un chargement sinusoïdale pour différentes théories est illustrée sur la figure 3, en remarquons que tous les modèle proposent présentent de bonne approximations. Les déplacements axiaux prédis par les modèles sont du même ordre de précision.

Aussi, il est remarqué qu'au niveau de la partie supérieure et inférieure des deux poutres une divergence des modèles FSDT et ETB par rapport à ceux du modèle de Reddy [18] ainsi que la présente théorie pour un rapport d'élancement $L/h = 4$ toutefois cette divergence diminue au fur et à mesure qu'on augmente le rapport d'élancement.

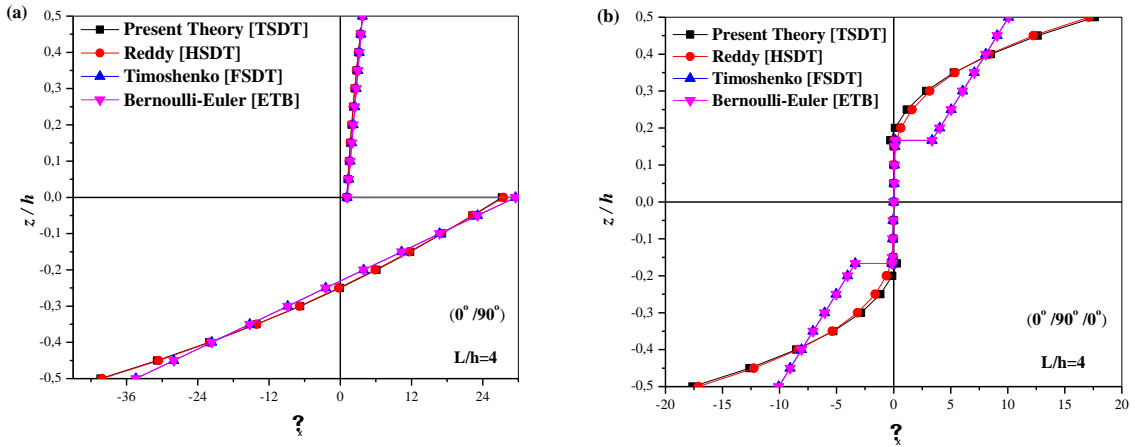


Figure 4 : Variation de la contrainte axiale σ_x à travers l'épaisseur de la poutre (0°/90°/0°) soumise à un chargement sinusoïdale pour un rapport d'élancement de $L/h = 4$.

La figure 4.a pour une poutre (0°/90°) soumise à un chargement sinusoïdale pour un rapport d'élancement de 4, montre que la contrainte axiale de flexion prédit par la présente théorie est en excellent accord avec celle de la solution exacte. La théorie de Reddy [18] donne la valeur plus élevée de la contrainte de flexion par rapport à la valeur exacte pour tous les aspects d'élancement alors que FSDT et ETB prédit une valeur inférieure pour la même chose.

Les figures 4.b montrent la variation de la contrainte axiale de flexion à travers l'épaisseur de la poutre (0°/90°/0°) soumise à un chargement sinusoïdale pour un rapport d'élancement de 4. On remarque que sur la fibre supérieure est une compression après elle devienne une traction sur la partie inférieure. On observe que sur la couche centrale, la contrainte est presque identique pour la poutre (0°/90°/0°).

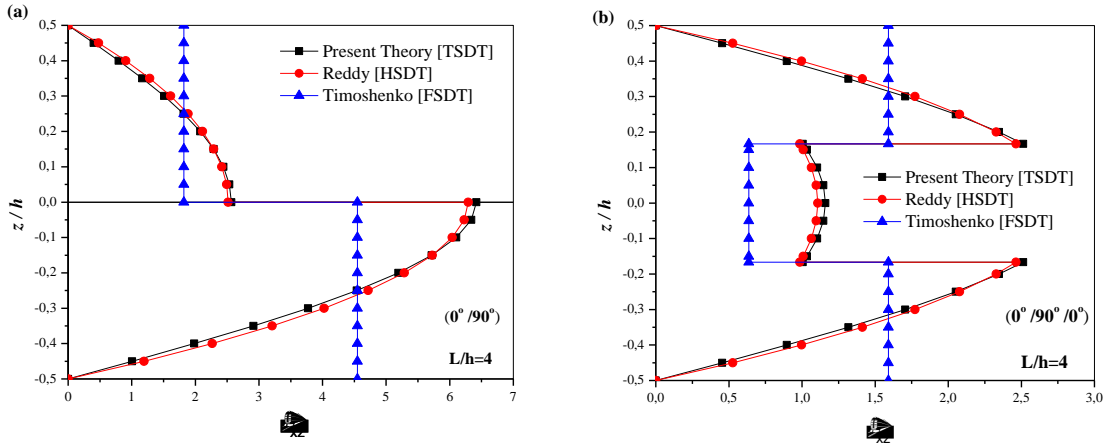


Figure 5 : Variation de la contrainte de cisaillement τ_{xz} à travers l'épaisseur de la poutre (0°/90°) soumise à un chargement sinusoïdale pour un rapport d'élancement de $L/h = 4$.

La contrainte de cisaillement transverse prédit par la présente théorie est en excellent accord pour le rapport d'élancement 4. Les contraintes de cisaillement ont une distribution parabolique sur l'épaisseur de la poutre et la théorie quasi-3D actuelle montre une bonne précision dans la prédition de la contrainte de cisaillement transverse par rapport à la solution exacte obtenue en utilisant l'équation d'équilibre (voir la figure 5). La contrainte de cisaillement transverse maximale prédite par la théorie de Reddy [18] est juste avec la solution exacte alors que FSDT et ETB surestiment lorsqu'il est obtenu en utilisant l'équation d'équilibre. Il est clair qu'au niveau de la fibre supérieure et inférieure de la poutre, la contrainte tangentielle est égale à zéro. On remarque aussi que la contrainte tangentielle est inférieure dans la couche centrale et cela est essentiellement dû à l'orientation des fibres pour (0°/90°/0°).

4. Conclusion

Dans cette recherche, nous avons présenté les résultats numériques de l'analyse du comportement élastique de la flexion des poutres en matériau composite en utilisant une nouvelle théorie à distribution hyperbolique de déformation de cisaillement.

La présente théorie à une forte similitude avec la théorie d'ordre élevée des poutres dans de nombreux aspects, n'exige pas de facteur de correction de cisaillement, et donne une description parabolique de la contrainte de cisaillement à travers l'épaisseur tout en remplissant la condition de contrainte de cisaillement nulle sur les bords libres.

Toutes les études comparatives ont démontrées que les flèches et les contraintes dues au chargement mécanique obtenues en utilisant la présente théorie et les autres théories de déformation de cisaillement d'ordre élevé ainsi que la théorie exacte sont presque identiques.

Par conséquent, on peut dire que la théorie proposée est précise pour résoudre le comportement élastique de la flexion des poutres.

REFERENCES

- [1] - Ambartsumian SA. On the theory of bending plates. Izv Otd Tech Nauk SSSR 1958; 5: 69–77.
- [2] - E. Reissner, “On the theory of bending of elastic plates,” J. Math. Phys., 23, 184-191 (1944).
- [3] - E. Reissner, “The effect of transverse shear deformation on the bending of elastic plates,” J. Appl. Mech., 12, 69 –77 (1945).
- [4] - Ghugal YM and Shimpi RP (2002). A review of refined shear deformation theories for isotropic and anisotropic laminated beams. Journal of Reinforced Plastics and Composites. 21: 775-813.
- [5] - Jones RM (1975). Mechanics of Composite Materials. McGraw Hill Kogakusha. Ltd. Tokyo
- [6] - Kant T and Manjunatha BS (1989). Refined Theories for Composite and Sandwich Beams with C0 Finite Elements. Computers and Structures. 33: 755–764.
- [7] - Karama M, Afaq KS and Mistou S. Mechanical behaviour of laminated composite beam by new multi-layered laminated composite structures model with transverse shear stress continuity. Int J Solids Struct 2003; 40: 1525–1546.
- [8] - Khdeir AA and Reddy JN (1997). An Exact Solution for the Bending of Thin and Thick Cross-ply Laminated Beams. Composite Structures. 37(2): 195–203.
- [9] - Levinson M. An accurate simple theory of static and dynamics of elastic plates. Mech Res Commun 1980; 7: 343–350.
- [10] - Lo KH, Christensen RM and Wu EM (1977a). A higher order theory for plate deformations, part 1: homogeneous plates. ASME Journal of Applied Mechanics. 44: 663–668.
- [11] - Lo KH, Christensen RM and Wu EM (1977b). A higher order theory for plate deformations, part 2: laminated plates. ASME Journal of Applied Mechanics. 44: 669–676.
- [12] - Maiti DK and Sinha PK (1994). Bending and Free Vibration Analysis of Shear Deformable Laminated Composite Beams by Finite Element Method. Composite Structures. 29: 421–431.
- [13] - Manjunatha BS and Kant T (1993a). New theories for symmetric/unsymmetric composite and sandwich beams with c0 finite elements. Composite Structures. 23: 61–73.
- [14] - Manjunatha BS and Kant T (1993b). Different numerical techniques for the estimation of multiaxial stresses in symmetric/unsymmetric composite and sandwich beams with refined theories. Journal of Reinforced Plastics and Composites. 12: 2–27.

- [15] - Muskhelishvili NI (1963). Some basic problems of the mathematical theory of elasticity. English Translation of 4th Ed., Noordhoff, Groningen, the Netherlands, Chap. 25.
- [16] - Pagano NJ (1969). Exact solution for composite laminates in cylindrical bending. *Journal of Composite Materials*. 3: 398–411.
- [17] - R. D. Mindlin, “Influence of rotatory inertia and shear on flexural motions of isotropic elastic plates,” *J. Appl. Mech.*, 18, 31–38 (1951).
- [18] - Reddy JN. Mechanics of laminated composite plates and shells: theory and analysis, 2nd ed. Boca Raton: CRC Press, 2004.
- [19] - Silverman IK (1964). Orthotropic beams under polynomial loads. *Journal of the Engineering Mechanics Division Proceedings of ASCE*. 90: 293–319.
- [20] - Soldatos KP and Elishoff I (1992). A transverse shear and normal deformable orthotropic beam theory. *Journal of Sound and Vibration*. 154(3); 528–533.
- [21] - Soldatos KP. A transverse shear deformation theory for homogeneous monoclinic plates. *Acta Mech* 1992; 94: 195–200.
- [22]- Thai HT, Vo TP. A new sinusoidal shear deformation theory for bending, buckling, and vibration of functionally graded plates. *Applied Mathematical Modelling* 2012a; doi: 10.1016/j.apm.2012.08.008.
- [23] - Thai HT, Vo TP. A size-dependent functionally graded sinusoidal plate model based on a modified couple stress theory. *Composite Structures* 2012b;doi: 10.1016/j.compstruct.2012.09.025.
- [24] - Touratier M. An efficient standard plate theory. *Int J Eng Sci* 1991; 29: 901–916.
- [25] - Vinayak RU, Prathap G and Naganarayana BP (1996). Beam Elements Based on a Higher Order Theory-I: Formulation and Analysis of Performance. *Computers and Structures*. 58: 775–789.



**Revue des Matériaux
&
Energies Renouvelable**

Journal home : www.cu-relizane.dz

ISSN : 2507-7554

E- ISSN : 2661-7595



Reliable Standalone Solar Battery Charging System Using ARDUINO Based on MPPT Controller

Open Access

Seddik ZEMITTE^{1*}, Messaoud HAMOUDA¹, Fatima Zohra ARAMA¹, Ahmed SAIDI²

¹laboratoire de Développement Durable et informatique (LDDI), Département des Sciences et Technologie ,université de adra, Algérie
²ENERGARID et SG&RE aboratoire, Département de génie électrique., universié de Bachar , Algérie

ABSTRACT

Article history:

Received March 21, 2020

Received in revised form March 22, 2020

Accepted July 09, 2020

Keys word: Solar Charger, DC- DC Buck, MPPT technical, Disturbance and Observation (P & O).

This paper aims to provide a study and a realization of a reliable standalone solar battery charging system, it is the main unit of the independent PV systems, used to manage the power sent from the photovoltaic panel to avoid damaging the battery, this one is a very sensitive device to charging / discharging. For this reason, a special control system (called charge regulator) is placed between the photovoltaic installation and batteries to maintain and optimize the functioning of the energy chain. The studied system consists of a photovoltaic module delivering 10w, and a static dc - dc converter of buck type, controlled by a rectangular signal PWM (pulse width modulation) by varying the duty cycle. the signal is generated by the ARDUINO-UNO board where the maximum power point tracking (MPPT) algorithm named perturb & observee (p & o) is implemented to charge a 12v battery, using the ISIS proteus software to make the virtual simulation of the different parts of the system before proceeding to the practical realization which results are satisfactory

Copyright © 2020 - All rights reserv

1. Introduction

In recent years, the trend toward a renewable energy system has drawn much attention as a clean source, non-polluting and cheaper than non-renewable energy formatters will need to create these components, incorporating the applicable criteria that follow the maximum power point [1][2]. One of the most important sources of renewable energy is photovoltaic energy(PV), to feed a load through a pv installation. It is often necessary to equip the system with storage batteries. batteries can store energy for use when needed. however, the connection of batteries with photovoltaic installations can present a poor performance because the batteries are very sensitive to overloads and deep discharges , it is therefore necessary to add an adaptation system called a charge controller to optimize the operation of the energy chain charge controllers based on the mppt command (maximum power point tracker) [3][4]. are modern regulators. not only are they able to monitor the charging / discharging of batteries. but they can force the pv generator generates its maximum power regardless of the variation in climatic conditions (temperature and sunshine) [5] nowadays, various methods are proposed [6][7]The most common methods of MPPT is incremental conductance , perturb and observe , fractional open voltage and fractional short-circuit current methods[8] , after that, many methods have been developed in this field especially that rely on artificial intelligence. The goal of our work is the electronic realization of a solar battery charging, the main device in standalone

* Corresponding author. Tel: +213666306645

E-mail address: sed.zemitte@univ-adrar.dz

photovoltaic systems that is used to manage the energy transmitted from the photovoltaic panel in order not to damage the battery, in this study we followed the technic p&o (perturb and observe). The PO technic operate by perturbing the reference value with specific sampling rates[9].a popular variation of the PO method [10] is based on the relationship of the PV array output power and the switching duty cycle. This method is defined as the hill climbing search (hcs) technic in[8][11]. The system to be studied consists of a photovoltaic module delivers a power of 10w, and a dc-dc buck type static converter controlled by a rectangular PWM type signal by varying the duty cycle which represents a control correlation between the conduction time and the total switching period. During its operations, the mosfet turns on and off until the maximum power point delivered by the module is reached. The signal is generated by the Arduino Uno board where the MPPT algorithm named disturbance and observation (P&O) is implemented to charge a 12v battery, using ISIS proteus software to do the simulation before proceeding to practical realization.

1.2. Paper contribution :

This paper develop a new generator charging system constitute of PV solar battery charger using UNO-ARDUIN controlled with classical MPPT technic and present the following points:

- Protect the battery from overcharging and under discharge limit.
- Force the PV generator generates its maximum power regardless of the variation in climatic conditions (temperature and sunshine).

2. Material And Method :

2.1. description of the photovoltaic conversion chain:

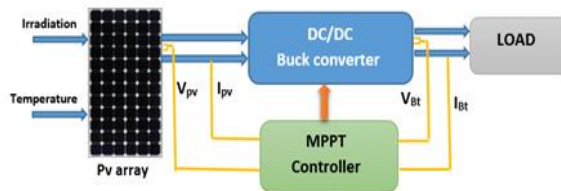


Figure 1 - PV system control structure.

The PV conversion chain is considered as a critical process in which reliable controls would improve the efficiency of the charging operation of connected storage batteries

figure 1 shows a simplified scheme of a standalone PV system with DC-DC buck converter.

2.2. Modeling of the photovoltaic cell :

The equivalent circuit of a photovoltaic cell is represented in figure 2, it is formed by a current generator supplying a current I_{ph} proportional to the light intensity, a diode modeling the PN junction and two resistors, the first is in series R_s representing the various contact resistances and the resistance of the semiconductor, the second resistor R_p parallel resistance characterizing the leakage current at the surface of the cell due to the non-ideality of the PN junction and impurities near the junction.

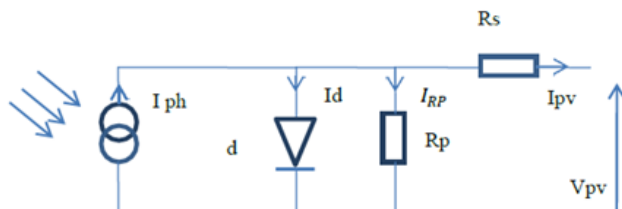


Figure 2-The equivalent circuit of photovoltaic cells

I_{pv} and V_{pv} are the output current and output voltage of the cell. applying kirchhoff's current law we can get the output current expression [12]

$$I_{pv} = I_{ph} - I_d - I_{Rp} \quad (01)$$

The current flowing through the diode is given by :

$$I_d = I_s * \left[e^{\frac{q*(V_{pv}+R_t*I_{pv})}{nkT}} - 1 \right] \quad (02)$$

Current flowing through resistor shunt

$$I_{Rp} = \frac{V_{pv} + R_s * I_{pv}}{R_p} \quad (03)$$

The formula of the photo-current

$$I_{ph} = [I_{cc} + K_1 * (T - T_{ref})] * \frac{G}{G_r} \quad (04)$$

The output current of the PV cell is given from the law of the nodes

$$I_{pv} = I_{ph} - I_s * \left[e^{\frac{q*(V_{pv}+R_t*I_{pv})}{nkT}} - 1 \right] - \left(\frac{V_{pv} + R_s * I_{pv}}{R_p} \right) \quad (05)$$

Where I_{ph} is the photo-generated current (A), I_s is the diode saturation current (A), V_{pv} is the Voltage at the terminals of the cell (V), I_{pv} is the output current of PV cell (A), R_s is the series resistance of the cell (Ω) and R_p is the shunt resistance of the cell (Ω). n is quality factor of the cell, K is the Boltzmann gas constant (1.38×10^{-23} J/K), q is the elementary charge (1.6×10^{-19} C), T is the absolute temperature of the cell (K), I_{cc} short circuit current (A), K_1 coefficient of temperature , T_{ref} reference temperature of the cell ($^{\circ}$ k) $T_{ref}=298$ K (25° C), G_r reference solar irradiation $G_r=1000$ w/ m², G solar irradiation of operation.

2.3. I-V and P-V characteristics:

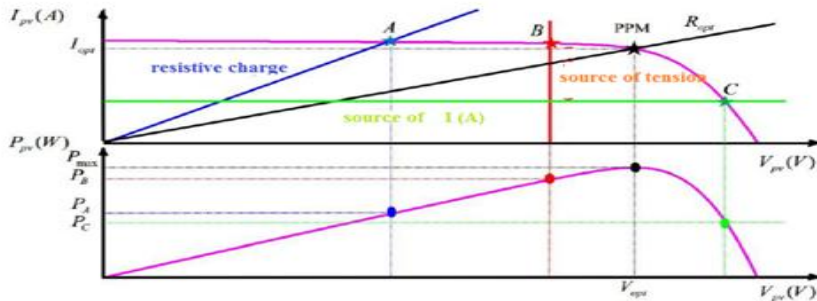


Figure 3-solar cell (current-voltage) and (power-voltage) characteristics

From Figure 3 we can see that the PV generator has a non-linear I-V correlation. And we can also notice that the generator can produce a maximum power at the point (V_{opt} , I_{opt}).

3.1. Influence of temperature and irradiance on the current / voltage characteristic :

The operation of the photovoltaic cell depends on the level of solar irradiance and the temperature of the cell. In this part, we will demonstrate the influence of changing weather conditions on the current and voltage generated by the solar panel.

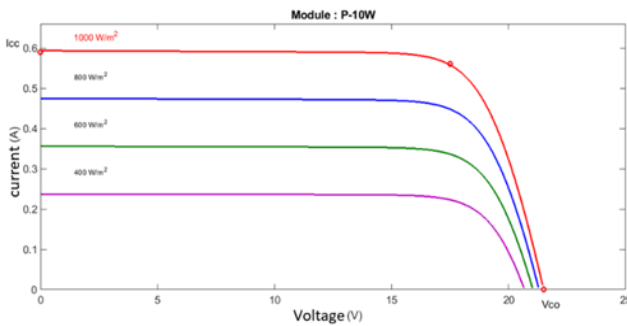


Figure 4- Influence of irradiance on current-voltage characteristic

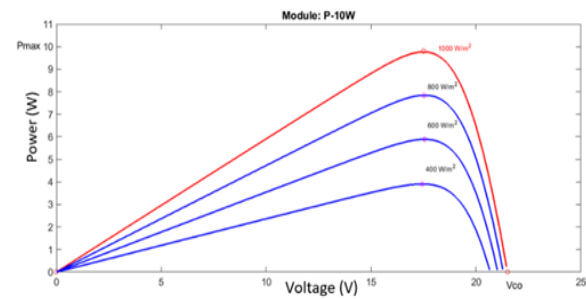


Figure 5- Influence of irradiance on the power-voltage characteristic

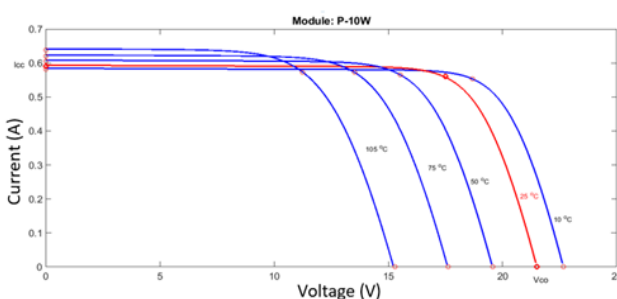


Figure 7- Influence of temperature on current-voltage characteristic

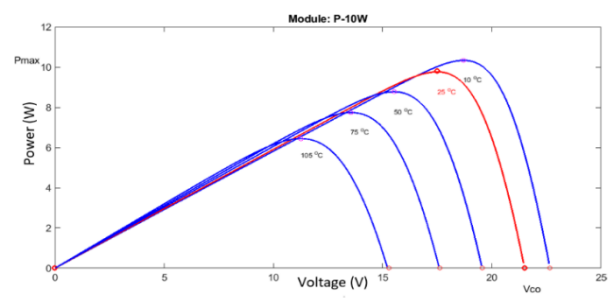


Figure 6- influence of temperature on power-voltage characteristic

From the figure 4 we can observe that the increase in solar irradiance causes the value of the short-circuit current to increase while the value of the open circuit voltage, varies very little. And figure 5 shows that the increase in solar irradiance causes the increase of the power of PV panel. On the other hand from the figure 6 we can observe that as the temperature increases and goes away from 25 °C the open circuit voltage V_{co} decreases, so the temperature has a negligible influence on the value of the short-circuit current. And figure 7 shows that when the temperature of the solar panels goes away from 25 °C the power diminishes.

2.4. Photovoltaic energy storage batteries:

A solar battery is intended to store the electrical energy in chemical form, used in photovoltaic systems because the demand for electricity does not coincide with the production because of the poor performance of the generator. The storage of energy is done to ensure the proper functioning of the system when solar energy is not sufficient or available.

There are several types of electrochemical accumulators (Pb, Ni-Cd, Li-ion, ...). However, the oldest and most commonly used are those made of lead and nickel cadmium. In the solar field, lead-acid batteries are the most used because they can withstand many cycles of charging and discharging without being damaged [13].

2.4.1. The battery charging cycle:

2.4.1.1. Normal cycle or Bulk charge:

Bulk charge is a constant current charging mode, it represents the first step of the charging cycle to follow where the photovoltaic panel charges a battery discharged by the maximum current allowed. During this charging mode the voltage across the battery gradually increases and ensures a quick recovery of the battery capacity

2.4.1.2. Equalization cycle or load absorption:

The Battery Voltage Must Be Maintained At The V_r Regulation Value In Order To Complete The Battery Charge And Avoid The Overload.[13]

2.4.1.3. End of charge or float charge:

This step is a step maintenance where the battery voltage is reduced to a fair enough level v_f to compensate self-discharge of the cells. And the charging current become very weak and almost constant, this is the state full charge.[13]

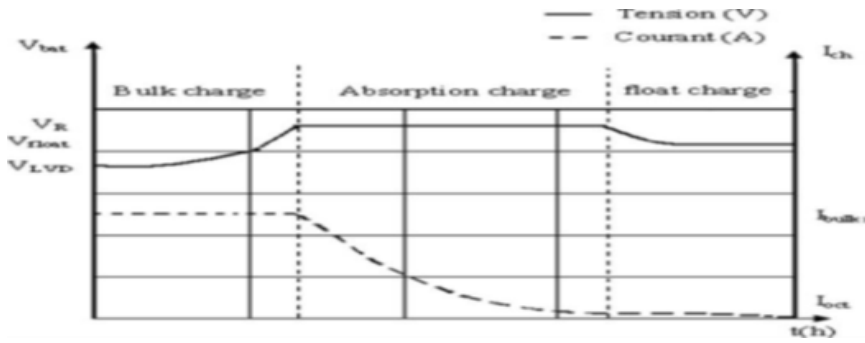


Figure 8 - Three-step charging algorithm

2.5. the purpose of inserting a charge controller :

The direct connection between the photovoltaic generator and the battery is simple to perform but does not offer good performance and has a poor performance because the batteries are very sensitive to charging / discharging, therefore the latter must not be too charged or too discharged as this influences their lifetime. It is necessary to ensure a better adaptation of an autonomous photovoltaic system with a battery, this is done through the insertion of a component named "MPPT battery charger" whose role and to maintain the life of the battery and force the generator to operate at its maximum power and transfer it to the battery which often suffers from a maladaptation because frequently, the operating point of the GPV is far from the maximum operating point because of the change of weather conditions and the variation of the state of charge of the battery.

2.6. Buck converter:

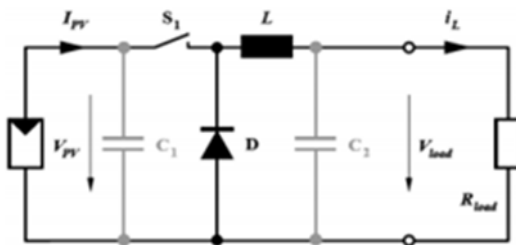


Figure 9 - Buck converter structure

Figure (9) shows the appearance of the pulse width modulated (PWM) signal of fixed frequency and variable pulse width which controls the switch S_1 . It is adjusted by the parameter α named the duty cycle in the time when the switch is closed (T_{on}) divided over the period of its switching T .

$$\alpha = \frac{T_{on}}{T} \quad (06)$$

$$T_{on} = \alpha T \quad (07)$$

Conduction time

$$T_{off} = (1 - \alpha) * T \quad (08)$$

Blocking time

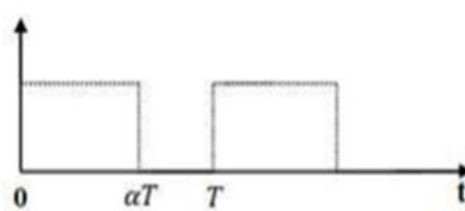


Figure 10 - Switch control signal

2.7. P&O MPPT algorithm :

The perturb and observe (P&O) algorithm is generally the most commonly applied in the control of MPPT algorithm for the PV generator. It has simple structure, low cost, easy to implement, reduced number of parameters, the possibility to introduce improvements and may result in top-level efficiency[14][15] This algorithm is depending on investigating the relation between PV module output power and its voltage. The behavior of solar panel indicating MPP and operating principle is shown in Fig. 11 which indicates that the resulting change of PV power is observed as follows: When the PV module operating point is on the left side of the curve ($\Delta P/\Delta V$ is positive), which means the PV module output power increases, the perturbation of the PV module voltage should be increased[16]

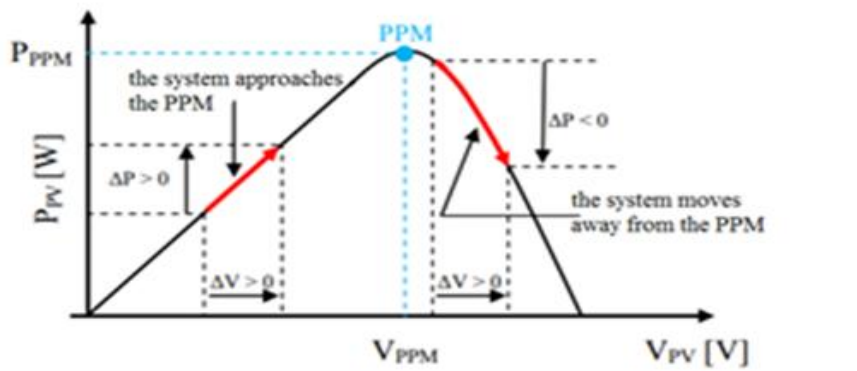


Figure 11 - Characteristic power - voltage of the photovoltaic generator

Figure (12) shows the classical algorithm associated with a P & O type MPPT control, where the evolution of the power is analyzed after each voltage disturbance. For this type of control, two sensors (current and voltage of the GPV) are necessary to determine the power of the PV at every moment.

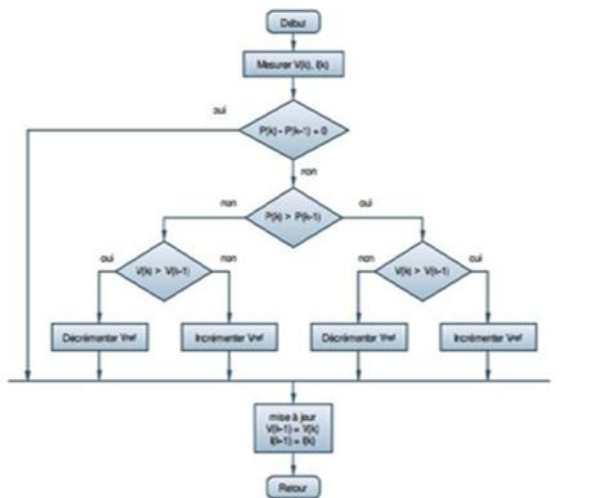


Figure 12 - Organizational chart of the disrupt & observe algorithm

3. Simulation :

Virtual simulation was done using ISIS Proteus to test the proper functioning of the system.

3.1. Simulation of the solar panel :

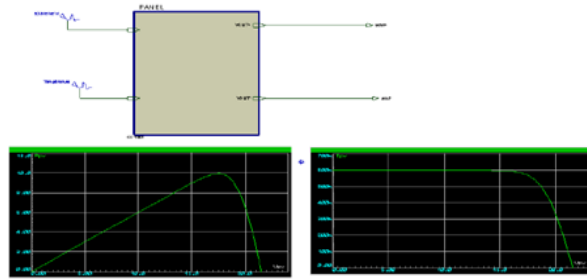


Figure 13 - Simulation of the solar panel used

3.2. Simulation of the control part:

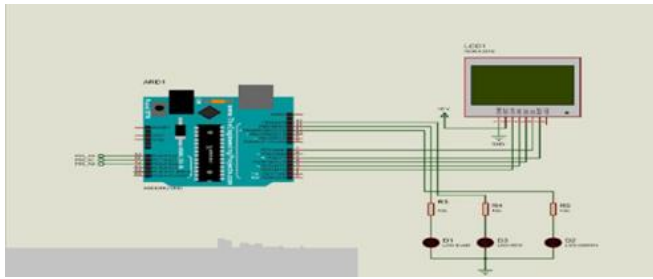


Figure 14 - Arduino Uno under ISIS PROTEUS

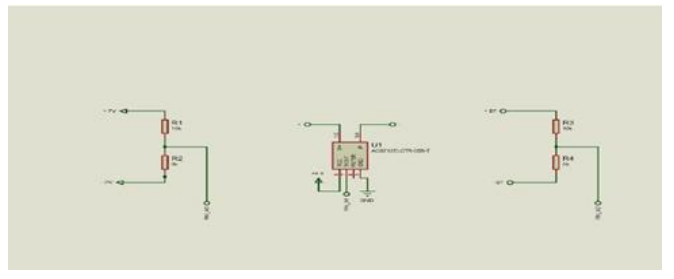


Figure 15 - Simulation of different sensors

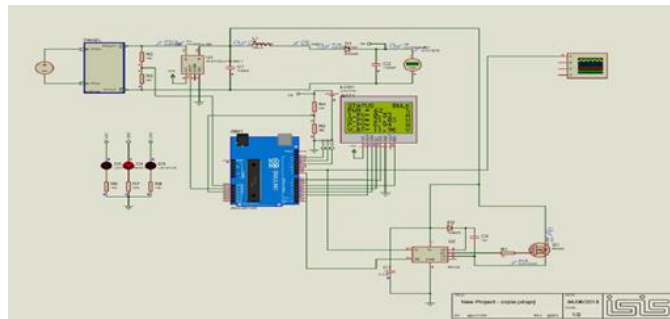


Figure 16 - Overall scheme of the device realized under ISIS Proteus

4. Results And Discussion:

4.1. Experimental trials :

After the simulation stage we are interested in the practical side in this case the control part by ignoring the presence of the power section. For this, we performed several tests with the four states of charge of the battery (On, Bulk, Float, Off). Knowing that the outputs of the solar panel are variable depending on the illumination and the ambient temperature, also the voltage at the terminals of the battery depends on the state of charge, we used potentiometers to get closer to the reality and the experimentation of three scenarios relating to the operation of the solar panel. as illustrated by the picture below, we have connected Arduino pin A0 to first potentiometer, representing the voltage across the solar panel, Pin A1 of the Arduino to the second potentiometer, representing the current generated by the panel solar and pin A2 of the Arduino to the third potentiometer, representing the voltage across the battery.

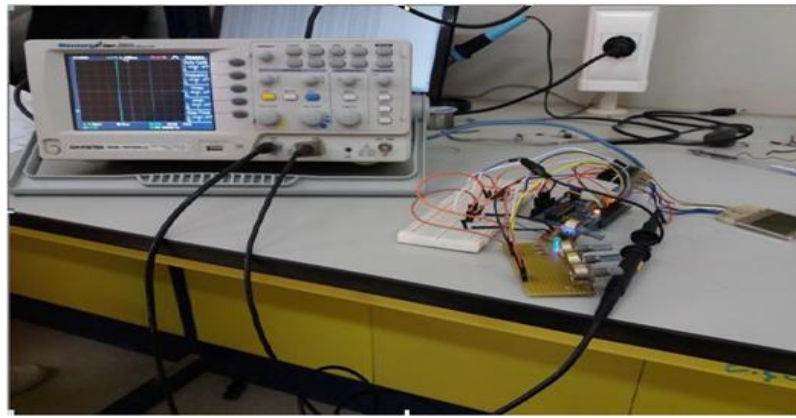


Figure 17 - Realization of the command part

4.2. First scenario "Constant temperature":

The temperature considered is 25°C , hence the outgoing voltage of the solar panel is optimal, 17.5 volts, while the illumination is variable, therefore the current obtained away from the optimal current given by the manufacturer of the panel, that is 0.56A.

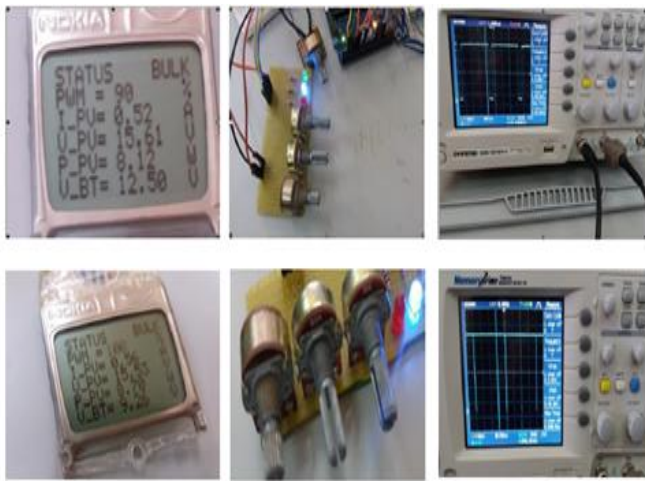
By applying different voltages to the battery, we found that the state of charge of the battery behaves according to the instructions of the program given to the lights, some pictures taken during the realization and an illustrative table of recorded data.

Table 1 results of the first scenario

$V_{PV} = 17.5 \text{ V}$					
Voltage of battery (V)	current (A)	Power (W)	duty cycle %	State of charge	Colors of the LEDs
≈ 9	0.1	2.79	100	ON	Green light
	0.2	3.49	100	ON	Green light
	0.3	5.24	63	BULK	Light blue
	0.4	6.99	61	BULK	Light blue
	0.5	8.74	60	BULK	Light blue
≈ 12	0.1	1.74	100	ON	Green light
	0.2	3.49	100	ON	Green light
	0.3	5.23	60	BULK	Light blue
	0.4	6.98	60	BULK	Light blue
	0.5	8.72	60	BULK	Light blue
≈ 14	0.1	1.75	100	FLOAT	All LEDs on
	0.2	3.84	100	FLOAT	All LEDs on
	0.3	5.24	63	FLOAT	All LEDs on
	0.4	6.99	61	FLOAT	All LEDs on
	0.5	8.74	60	FLOAT	All LEDs on
≈ 16	0.1	1.74	60	OFF	Red light
	0.2	3.49	60	OFF	Red light
	0.3	5.23	60	OFF	Red light
	0.4	6.98	60	OFF	Red light
	0.5	8.72	60	OFF	Red light

4.3. Second scenario "Constant illumination"

The illumination considered is 1000W/m^2 , hence the current coming out of the panel Solar is optimal, that is to say 0.56A, whereas the temperature is variable part consequently the obtained voltage moves away from the optimal voltage given by the panel manufacturer, or 17.5Volts. Applying different voltages to the battery, we found that the state of battery charge behaves according to the instructions of the program data the indicator lights below, the figure below shows some pictures taken during the realization and all the data recorded in the table (2).

Table 2 results of the second scenario**Figure 18 - Pictures taken from the second scenario**

$I_{PV} = 0.55 \text{ A}$					
Voltage of battery (V)	Voltage panel (V)	Power (W)	duty cycle %	State of charge	Colors of the LEDs
≈ 9	15.01	7.81	77	BULK	Light blue
	15.61	8.12	80	BULK	Light blue
	16.04	8.34	75	BULK	Light blue
	16.63	8.65	81	BULK	Light blue
≈ 12	15.01	7.81	85	BULK	Light blue
	15.61	8.12	90	BULK	Light blue
	16.04	8.36	89	BULK	Light blue
	16.63	8.85	93	BULK	Light blue
≈ 14	15.01	7.82	60	FLOAT	All LEDs on
	15.61	8.12	60	FLOAT	All LEDs on
	16.04	8.36	60	FLOAT	All LEDs on
	16.63	8.66	60	FLOAT	All LEDs on

When a voltage of 15 volts is applied, the power obtained is sufficient for the battery to be in the "Bulk" position, which is quickly charged with the maximum power using the disturbance and observation method.

The algorithm continues its calculations until reaching the maximum voltage across the battery. All the indicator lights come on, this is the position "Float" or end of charging the battery, then a loop of the program ensures the protection of the battery by disconnecting the GPV to avoid its overload and the warning light is red.

4.4. Third scenario "Variation of irradiance and temperature"

The purpose of this scenario is to verify the behavior of the program with respect to variations in climatic conditions, including illumination and temperature at the same time, as well as their impact on the current and voltage generated by the solar panel. By applying different voltages to the battery, we found that the state of the battery behaves according to the instructions of the program. As shown in the figure below and Table III gives the different responses of the system due to the random variations of two parameters influencing at the same time the characteristic of the panel .

Table 3 results of the third scenario

Voltage of battery (V)	Voltage and current panel (V and A)	Power (W)	duty cycle %	State of charge	Colors of the LEDs
≈ 9	(17.50V – 0.56A)	9.86	83	BULK	Light blue
	(12.23V – 0.30A)	3.67	100	ON	Green light
	(17.23V – 0.20A)	3.45	100	ON	Green light
	(13.00V – 0.56A)	7.67	75	BULK	Light blue
≈ 12	(17.50V – 0.56A)	9.86	99	BULK	Light blue
	(12.23V – 0.30A)	3.77	100	ON	Green light
	(17.23V – 0.20A)	3.45	100	ON	Green light
	(13.00V – 0.56A)	9.66	80	BULK	Light blue
≈ 14	(17.50V – 0.56A)	9.86	60	FLOAT	All LEDs on
	(12.23V – 0.30A)	3.67	60	FLOAT	All LEDs on
	(17.23V – 0.20A)	3.44	60	FLOAT	All LEDs on
	(13.00V – 0.56A)	7.38	60	FLOAT	All LEDs on

From Table 3 we find that When we apply an optimal voltage and current(17.50V – 0.56A), the power obtained is sufficient for the battery to be in the "Bulk" position and the battery is charged quickly with the maximum power, and When we apply a weak voltage and current the power obtained is not sufficient for the battery to be in the "Bulk" position and this one will be in the "ON" position with the stepwise running of the program until the maximum voltage is reached, While when we apply a low voltage and an optimal current, the power obtained is sufficient for the battery to be in the "Bulk" position and the battery is charged quickly with maximum power, and When we apply a an optimum voltage and a low

current, the power obtained is not sufficient for the battery to be in the "Bulk" position and the latter will be in the "ON" position with the step-by-step program until the maximum voltage is reached. The algorithm continues its calculations until reaching the maximum voltage across the battery, all the lights come on, this is the position "Float" or end of charging the battery, by the another protection loop ensures the automatic disconnection of the battery and the indicator light is red

5. Conclusion :

This paper presented a simulated and experimental study of the realization of a reliable standalone solar battery charging system capable of tracking the maximum power point using a perturb & observe technic in very low cost .

The experimental results in tables 1, 2 and 3 shows the system response at different stages of battery charging and ensure that storage batteries are protected from overcharging and under discharge limit as well as improving the efficiency of the photovoltaic generator.

The use of an ARDUINO UNO has reduced the expense of additional circuits needed to protect the storage element. Instead of using expensive sensors for current and voltage sensing, simple and cheap circuits using resistors are used.

REFERENCES

- [1]- S. Djørup, J. Z. Thellufsen, and P. Sorknæs, "The electricity market in a renewable energy system," Energy, 2018.
- [2]- Y. Aljarhizi, "Control Management System of a Lithium-ion Battery Charger Based MPPT algorithm and Voltage Control," 2019.
- [3]- S. Saravanan and N. Ramesh Babu, "Maximum power point tracking algorithms for photovoltaic system - A review," Renew. Sustain. Energy Rev., vol. 57, pp. 192–204, 2016.
- [4]- L. Liu, X. Meng, and C. Liu, "A review of maximum power point tracking methods of PV power system at uniform and partial shading," Renew. Sustain. Energy Rev., vol. 53, pp. 1500–1507, 2016.
- [5]- T. Nadu, T. Nadu, T. Nadu, and T. Nadu, "A Novel Approach on MPPT Algorithm for Solar Panel using Buck Boost Converter," pp. 396–399, 2016.
- [6]- D. P. Hohm and M. E. Ropp, "Comparative study of maximum power point tracking algorithms using an experimental, programmable, maximum power point tracking test bed," Conf. Rec. IEEE Photovolt. Spec. Conf., vol. 2000-Janua, pp. 1699–1702, 2000.
- [7]- I. W. Christopher and R. Ramesh, "Open Access Comparative Study of P & O and InC MPPT Algorithms," vol. 408, no. 12, pp. 402–408, 2013.
- [8]- M. B. Danoune, A. Djafour, and A. Gougui, "Study and Performance Analysis of Three Conventional MPPT Algorithms Used in Photovoltaic Applications," 2018.
- [9]- X. Liu and L. A. C. Lopes, "An improved perturbation and observation maximum power point tracking algorithm for PV arrays," PESC Rec. - IEEE Annu. Power Electron. Spec. Conf., vol. 3, pp. 2005–2010, 2004.
- [10]- E. Koutroulis, K. Kalaitzakis, and N. C. Voulgaris, "Development of a Microcontroller-Based , Photovoltaic Maximum Power Point Tracking Control System," vol. 16, no. 1, pp. 46–54, 2001.
- [11]- T. Senju and K. Uezato, "Maximum power point tracker using fuzzy control for photovoltaic arrays," pp. 143–147, 2002.
- [12]- M. B. Danoune, A. Djafour, A. Gougui, and N. Khelfaoui, "Characterization Of Photovoltaic Panel Using Single Diode And Double Diode Models A Comparative Study With Experimental Validation," no. October, 2018.
- [13]- M. S. A. Cheikh, M. C. Belhadj, M. Bassaid, and M. B. C. Larbès, "Simulation et réalisation d'un contrôleur de batterie solaire à base de PIC16F876," vol. 2, pp. 1–9, 2012.
- [14]- M. A. Elgendi, B. Zahawi, S. Member, and D. J. Atkinson, "Assessment of Perturb and Observe MPPT Algorithm Implementation Technics for PV Pumping Applications," vol. 3, no. 1, pp. 21–33, 2012.
- [15]- G. R. Patel, D. B. Patel, and K. M. Paghdal, "ANALYSIS OF P & O MPPT ALGORITHM FOR PV SYSTEM I . INTRODUCTION II . BASIC PRINCIPLE OF MPPT III . SYSTEM CONFIGURATION," vol. 5, no. 6, pp. 1–10, 2016.
- [16]- S. A. Mohamed and M. Abd El Sattar, "A comparative study of P&O and INC maximum power point tracking techniques for grid-connected PV systems," SN Appl. Sci., vol. 1, no. 2, pp. 1–13, 2019.



Revue des Matériaux & Energies Renouvelable

Journal home : www.cu-relizane.dz

ISSN : 2507-7554

E- ISSN : 2661-7595



Magnetic investigation of the rhodium based full-heusler material: ab initio Method

Open Access

BOUFADI Fatima Zohra ^{1*}

¹ Laboratory Physical and chemical of advanced materials LPCMA, Department of Physic, University Djillali Liabes of Sidi Bel Abbes

Article history:

Received 18 April 2020

Received in revised form ... 18 April 2020...

Accepted 02 August 2020

Keys word: Ab Initio Calculations - Heusler Alloy

- Spin - Polarization - Density of State – DFT

RESUME

In recent years, heusler alloys have attracted extensive attention because of their usefulness in spintronic devices. In this paper, the structural, electronic, and magnetic properties of full heusler alloys Rh₂MnZn have been studied by using the FPLAPW method based on density functional theory DFT. Calculations have been done by GGA. The investigations on the structural properties of the alloy showed that the rh2mzn alloy had a stable structure. The results of gga calculation on electronic properties of rh2mzn alloy show that the Rh₂MnZn alloy had metallic nature due to overlapping between conduction and valance band at fermi level for both spin directions. By studying the magnetic properties, we found that the Rh₂MnZn alloy were ferromagnetic materials. We showed that the compound Rh₂MnZn has a technological potential for spintronics.

Copyright © 2020 - All rights reserved

1. Introduction :

Magnetic materials underpin modern technologies, ranging from data storage to energy conversion to contactless sensing. However, the development of a new high-performance magnet is a long and often unpredictable process, and only about two dozen magnets are featured in mainstream applications. Full-Heusler which exhibit metallic character, the magnetic interaction is usually based on the m-J paradigm, where localized magnetic moments, m-J paramagnetically coupled through the exchange interaction, J. Only a few elements in the periodic table can provide localized moments in the solid state, namely, 3d transition metals, 4f rare earths, and some 4d ions. These materials have attracted great attentions due to their potential applications in spintronic devices, such as magnetic sensors, tunnel junctions, and giant magneto-resistance (GMR) [1, 2].

Heusler alloys are attractive because of their technical applications (in spin-injection devices [3], spin-filters [4], tunnel junctions [5], or GMR devices [6,7], their relatively high Curie temperature compared to other compounds, and their crystal structure similar to conventional semiconductors (zinc-blende and rock-salt types) [8–10]. In order to stabilise Heusler alloys practically, they should be grown on suitable substrates. Because Heusler alloys consist of 4 FCC sublattice, conventional semiconductors with zinc-blende structure (including 2 FCC sublattice) can be used as the substrate. The mismatch between thinfilm (Heusler alloys) and the substrate (semiconductors) should be as small as possible to keep the HM character of Heusler alloys in the growth process. Therefore, the lattice constant of the semiconductors must be chosen close to that of the Heusler alloys.

Heusler compounds generally take a cubic crystal structure with a 2:1:1 stoichiometry (X₂YZ) in which X and Y mainly are transition metals and Z is a main group element. X₂YZ Heusler compounds can be characterised with two different types: (1) the cubic L21 structure with a space group *Fm.3m* with prototype of AlCu₂Mn (Fig. 1) in which X, Y, and Z atoms are placed on the Wyckoff positions 8c (1/4, 1/4, 1/4), 4a (zero, zero, 0), and 4b (1/2, 1/2, 1/2), respectively. The second type is the CuHg₂Ti-type structure with a space group *F .43m* in which X atoms occupy the nonequivalent 4a (0, 0, 0) and 4c (1/4, 1/4, 1/4) positions, while Y and Z atoms are located at 4b (1/2, 1/2, 1/2) and 4d (3/4, 3/4, 3/4) positions, respectively [11]. In this structure, X atoms are denoted as X (1) and X (2).

*BOUFADI Fatima Zohra. E-mail address: fboufadi1978@gmail.com

The first part of this work consists in determining the structure and the most stable magnetic phase, a study of the structural and magnetic stability was based on the procedure of the adjustment on the equation of Birch- Murnaghan [12]. The second part includes the study of the electronic properties. Finally, we study the magnetic properties of this compound: Rh₂MnZn

2. Computational method :

The calculations were performed using the full-potential linearised augmented plane-wave (FP-LAPW) method within density functional theory (DFT) as implemented in the Wien2k package [13]. The exchange correlation potential (VXC) within the local density approximation (LDA) is calculated using the scheme of Ceperley–Alder as parametrised by Perdew–Zunger [14] and within the generalised gradient approximation (GGA) using the scheme of Perdew–Burke–Ernzerhof (PBE-GGA) [15]. In this method, the crystal is divided into nonoverlapping muffin-tin (MT) spheres surrounding the atomic sites and the interstitial regions among MT spheres. The wave functions are expanded terms of spherical harmonic functions inside MT spheres and in Fourier series in the interstitial region. The MT sphere radius for all atoms was chosen as two a.u. The potential function and charge density inside the MT spheres were expanded up to $l_{\text{max}} = 10$ and the largest vector in Fourier expansion of the charge density was $G_{\text{max}} = 12 \text{ (a.u.)}^{-1}$. The maximum value of the reciprocal lattice vector in the plane-wave expansion in the interstitial region (K_{max}) was determined to be equal to $8/R_{\text{MT}}$, where R_{MT} is the smallest MT sphere radius. The separation energy of the valence and the core electrons was chosen as -6 Ry . A mesh of 84 special k -points was made in the irreducible wedge of the Brillouin zone (Fig. 2). Self-consistency was achieved by setting the convergence of the charge smaller than $10^{-5} \text{ e/(a.u.)}^3$.

3. Results and discussion :

3.1. Structural properties :

In the first, The purpose of our study is to determine the most stable phase of the Rh₂MnZn Full-Heusler alloy and for this we performed calculations of the structural, electronic, magnetic, elastic and thermodynamic properties of this compound, using the code WIEN2k [1]. The WIEN2k code algorithm is based on the DFT density functional theory [16], which is a direct application of the FP-LAPW method [17]. Our calculations were based on the generalized gradient approximation (GGA) parameterized by Perdew, Burk and Ernzerhof [18]. The latter calculates the self-consistent solution of the Kohn and Sham equations [19], which describes the valence electron in a potential created by a periodic network.

To determine the most stable structure and the magnetic phase of the compound Rh₂MnZn, we carried out structural optimizations of this type of structure, for two magnetic phases: the nonmagnetic phase (NM) and the ferromagnetic phase (FM).

The structural optimization was performed by minimizing the total energy E as a function of volume V. the optimization cycle was reproduced until the imposed convergence is obtained. The modulus of compressibility at equilibrium was evaluated by adjusting the curve of variation of energy as a function of volume on the Birtch - Murnaghan equation [12] given by:

Where $E(V)$ represents the ground state energy with a cell volume V , and V_0 the volume of the unit cell at zero pressure, B_0 and B'_0 are the compressibility modulus and its derivative, respectively.

Fig. 3 shows the total energy in its magnetic (ferromagnetic, non-magnetic) phases as a function of volume for Rh₂MnZn. Table 1 shows the values obtained from the structural properties of Rh₂MnZn compound. Our calculations with GGA show that the ferromagnetic phase is the most energy stable for the studied alloy.

3.2. Electronic properties :

We calculated the band structures and the total and partial electronic densities of our compound; Rh₂MnZn, at its fundamental structural states for the majority and minority spins along the high symmetry directions in the first Brillouin zone, using the generalized gradient approximation (GGA-PBE).

The majority and minority spin band structures for the compound Rh₂MnZn are shown in Fig.4 and the Fermi level (E_f) was indicated by a black horizontal line. To understand the electronic properties of the studied alloy, the electronic band structures are calculated along the directions of high symmetry in the first Brillouin zone, shown in this Fig.4.

In the majority and minority spins, we notice that there is overlap between the conduction and valence bands, which means that this compound has a metallic character with the GGA approximation (PBE). This results in the absence of gap in both paths (spin-up, and spin-down). We note that there is a similarity in the band structures, in the two spin states (up and down).

The state density counts the number of electronic states having a given energy. The total state density allows, for example, having access to the electronic conduction properties of a material. In addition, for each atom, a sphere of given radius is defined, inside which the electron density is projected onto spherical harmonics of type (s, p, d or f). Partial state densities are thus obtained which make it possible to determine the structure of the chemical bonds between the atoms of a crystal or a molecule. The projections of the total state density depend on the radii of the spheres on which the partial state densities are projected and therefore only give access to qualitative information [20].

The total and partial state densities of compound Rh₂MnZn, obtained using the generalized gradient approximation (GGA), are illustrated in Fig. 5. The results show that the Fermi level is occupied by the d states of the Mn atom and the d states of

Rh in both the majority and minority spins. Around this level, the contribution of the states Mn-d, behaves differently, in the two directions of spin.

3.3. Magnetic properties :

The total and partial magnetic moments calculated using GGA are summarized in the table. We note that the total magnetic moments of spin are not integer values. Thus, the Rh₂MnZn alloy is not a Half Metallic material and it does not obey Slater's rule [21]: $M_{tot} = Z_T - 24$, or M_{tot} represents the total magnetic moment (in μB) per unit of formula and Z_T represents the total number of valence electrons. In addition, from its densities of states up and down, the values of the spin polarization of compound Rh₂MnZn are calculated.

In order to study the magnetic properties of the Heusler Rh₂MnZn alloy, we present the spin density distributions (spin-up charge density minus spin-down charge density) of the conventional four-unit mesh in the figure. IV.5. From this figure, we can notice that the spin moments are located around the Mn atoms. In addition, blue iso-surfaces with a positive spin density of $0.065 / \text{A}^3$ indicate that the Mn atoms are ferromagnetically coupled with Rh. The Mn atom has a significant spin comparing to the atoms of Rh and Zn. In detail, the rounded corners of the bumps for the Mn atoms are prominent. However, the magnetic moment of the atom of Mn is greater than that of the atom of Rh and Zn.

For this compound, there is no spin accumulated around the Rh and Zn atoms, demonstrating that the contribution to the total magnetic moments of these atoms is negligible. These results are consistent with the calculated total and atomic magnetic moments of the Rh₂MnZn alloy, (see Table 2).

4. Conclusion :

The objective of this work is the theoretical study of the structural, magnetic electronic properties of the Full Heusler Rh₂MnZn alloy, using the linearized augmented plane waves method at full potential (FP-LAPW) implemented in the WIEN2K code. The exchange and correlation effects are treated in the context of the generalized gradient approximation (GGA).

This type of material is much more popular than other classes of ferromagnetic alloys in magneto-electronic applications. The main results obtained indicate that this material studied in the direct phase (Cu₂MnAl) shows that the ferromagnetic phase is the most stable. Our calculations confirm the possibility of synthesizing this material experimentally. For the electronic properties, the band structures, the densities of the partial and total states were calculated. The application of the approximation (GGA with spin) shows that our compound is a ferromagnetic metal. The band structures in the two spin channels (up and down), at equilibrium state, indicate the metallic character, represented by the overlapping of the bands at the Fermi level. The densities of total and partial states show that the Fermi level is occupied by the *d* states of the Mn atom and the *d* states of the Rh atom in both the majority and minority spins. Densities in the valence band below Fermi level are mainly due to hybridizations of the orbitals of Mn atoms with Rh-*d*. Magnetic properties: total magnetic moments of spin are not whole values. Therefore, the alloy is not an HM material and does not obey the Heusler rule [22]. In addition, the spin polarizations of the compounds are 57.8%.

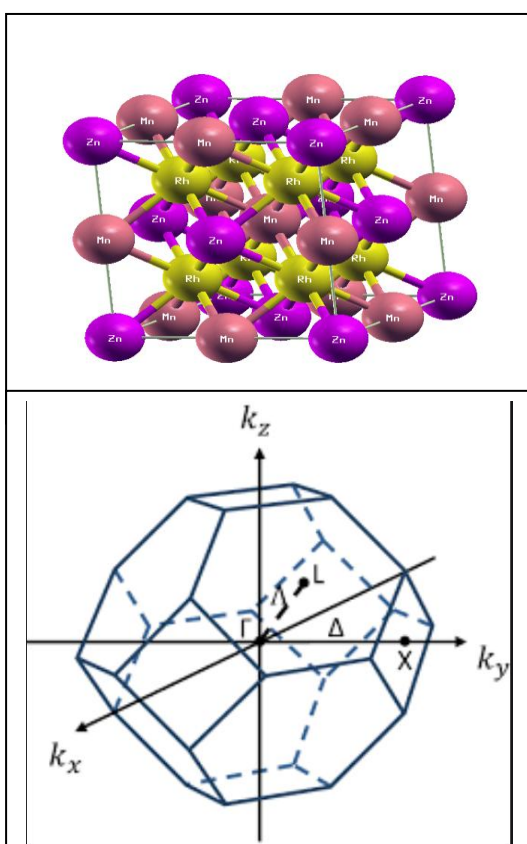


Fig. 1 : Maille conventionnelle : la AlCu₂Mn de composé Rh₂MnZn

structure Full-Heusler ordinaire (type

Fig. 2 Zone de Brillouin

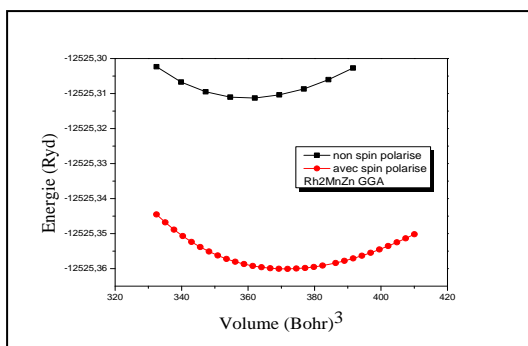


Fig. 3: Total energy of the Rh₂MnZn alloy as a function of volume of the elementary cell in the two magnetic phases FM and NM.

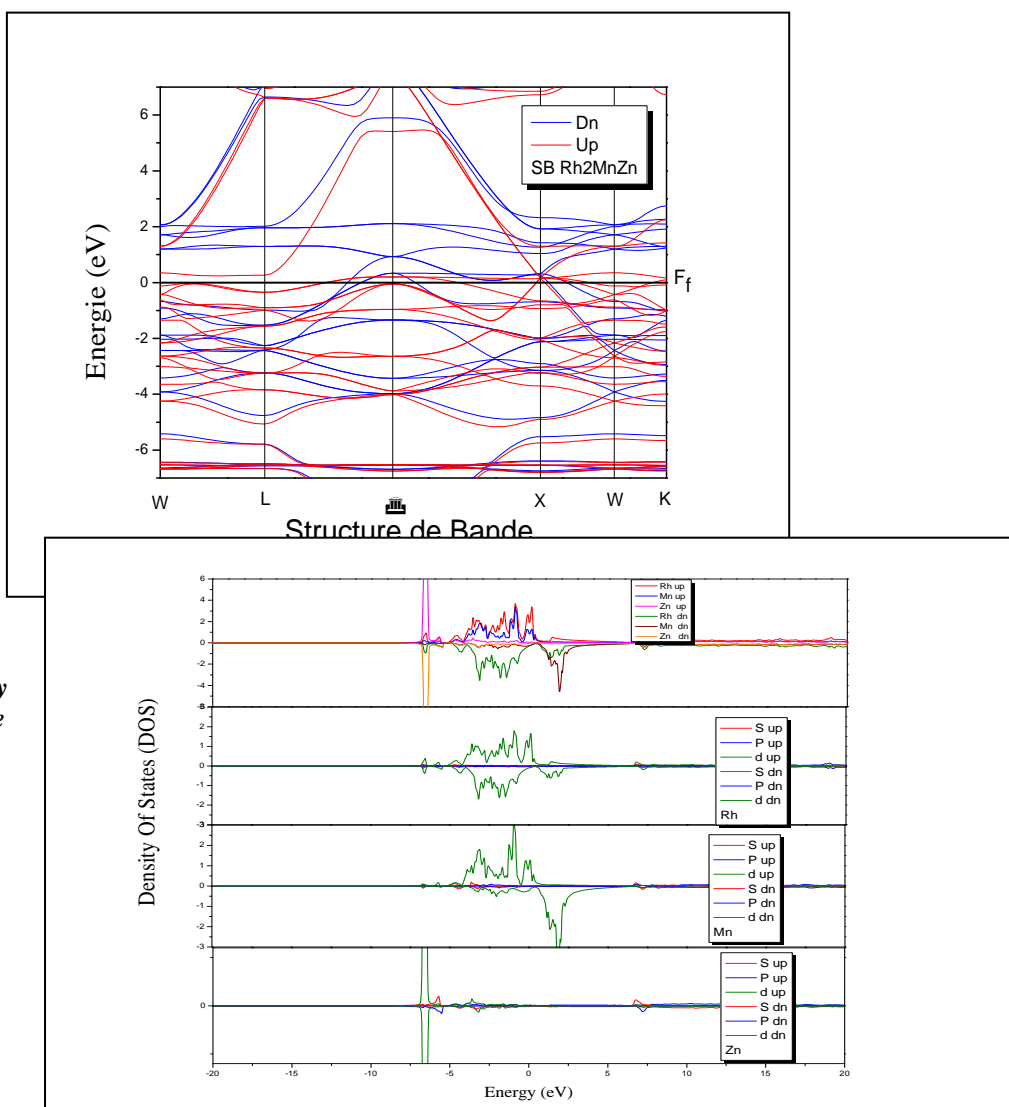


Fig. 5: Total and partial state densities of majority and minority spins of the Full-Heusler Rh₂MnZn alloy

$$E(V) = E_0 + \frac{9V_0B_0}{16} \left\{ \left[\left(\frac{V_0}{V} \right)^{2/3} - 1 \right]^3 B'_0 + \left[\left(\frac{V_0}{V} \right)^{2/3} - 1 \right]^2 \left[6 - 4 \left(\frac{V_0}{V} \right)^{2/3} \right] \right\} \quad (1)$$

$$P = \frac{\rho(\uparrow) - \rho(\downarrow)}{\rho(\uparrow) + \rho(\downarrow)} \quad (2)$$

Table 1: Structural properties of the Rh₂MnZn alloy (cell parameter a_0 , compressibility modulus B_0 , its derivative B'_0 , and the energy E_0).

<i>Rh₂MnZn</i>		Results	a_0 (Å)	B_0 (GPa)	B'_0	V_0 (u.a.) ³	E_0 (Ry)
	GGA	Ours	5,9756	214,1809	4,7712	359,9891	-25050,622527
		Others	/	/	/	/	/
	GGA (with spin)	Ours	6 .0357	176.5512	5.3268	371.3325	-25050.720128
		Others	6.03 ^[23]	/	/	371.28 ^[23]	/

Table 2: Total and partial magnetic moments in μB and the spin polarization for the Rh₂MnZn alloy

<i>Rh₂MnZn</i>	Results	M_{tot}	M_{int}	M_{Rh}	M_{Mn}	M_{Zn}	$\rho(\uparrow)$	$\rho(\downarrow)$	P (%)
	Ours	3.29810	0,01823	0.03524	3.22827	-0.01881	/	/	/
	Others	3.37 ^[23]	/	/	/	/	/	/	/

REFERENCES

- [01]- M. Jullier, 1975, Tunneling between ferromagnetic films, Phys. Institut national de sciences appliquées, 35031 Rennes Cedex, France. Lett. A54, 255.
 [02]- le magazine d'information de l'université Paris-sud, janvier-février 2008 numéro 69.

Magnetic investigation of the rhodium based full-heusler material: ab initio Method

BOUFADI Fatima Zohra

- [03]- H. C. Kandpal, G. H. Fecher, and C. Felser, 2007, “Calculated electronic and magnetic properties of the half-metallic, transition metal based Heusler compounds,” *J. Phys. Appl. Phys.*, vol. 40, no. 6, pp. 1507–1523.
- [04]- R. A. de Groot and F. M. Mueller, 1983, “New Class of Materials: Half-Metallic Ferromagnets,” *Phys. Rev. Lett.*, vol. 50, no. 25, pp. 2024–2027.
- [05]- Seddik Larbi, 2010, Mémoire de Magister en Science et génie des Matériaux, Université Djillali Liabes de Sidi-bel-Abbes.
- [06]- P. Grünberg, R. Schreiber, Y. Pang, M.B. Brodsky, H. Sowers, 1986 ,Characterization of Fat Fractals in Nonlinear Dynamical Systems, *Phys Rev. Lett.* 57, pp 2442.
- [07]- M.N. Baibich, J.M. Broto, A. Fert, F. Nguyen van Dau, F. Petroff P.Etienne, 1988, *Phys Rev Lett* 61, pp 2472.
- [08]- R. A. de Groot and F. M. Mueller, 1983, “New Class of Materials: Half-Metallic Ferromagnets,” *Phys. Rev. Lett.*, vol. 50, no. 25, pp. 2024–2027.
- [09]- F. J. Albert, J. A. Katine, R. A. Burhan, and D. C. Ralph, 2000, *Appl. Phys. Lett.* 77, 3809.
- [10]- Hongzhi Luo, Zhiyong Zhu, Guodong Liu, Shifeng Xu, Guangheng Wu, Heyan Liu, Jingping Qu, Yangzian Li, 2007, Journal of magnétisme and magnétic matérials, Tianjin 300130, PR China.
- [11]- S. Fujii, M. Okada, S. Ishida and S. Asano, 2008, *J. Phys. Soc. Jpn* 77, pp 74702.
- [12] F. Birch, 1978, *Journal of Geophysical Research: Solid Earth*, Finite strain isotherm and velocities for single-crystal and polycrystalline NaCl at high pressures and 300 K83 (B3), pp 1257-1268.
- [13] T. Ouahrani, 2011, calcul des propriétés structurales, thermiques et optiques des composés chalcopyrites par la méthode FP-(L) APW, Citeseer.
- [14] J. P. Perdew and A. Zunger, (1981). *Phys. Rev. B* **23**, 50484, <https://doi.org/10.1103/PhysRevB.23.5048>
- [15] J. P. Perdew, K. Burke, and M. Ernzerhof, 1996, *Phys. Rev. Lett.* **77**, 3865, <https://doi.org/10.1103/PhysRevLett.77.3865>.
- [16] R. Parr & W. Yang, 1989, in *Density Functional Theory of Atoms and Molecules* (Oxford University Press, New York).
- [17] D. Hamann, 1979, Semiconductor charge densities with hard-core and soft-core pseudo-potentials, *Physical Review Letters* 42(10), pp 662.
- [18] J.P. Perdew, K. Burke, M. Ernzerhof, 1996, Generalized gradient approximation made simple, *Physical Review Letters* 77(18), pp 3865.
- [19] W. Kohn, 1986, Density-functional theory for excited states in a quasi-local-density approximation, *Physical Review A* 34(2), pp 737.
- [20] T. Ouahrani, 2011, Calcul des propriétés structurales, thermiques et optiques des composés chalcopyrites par la méthode FP-(L) APW, Citeseer.
- [21] N. Cusack, *The electrical and magnetic properties of solids: an introductory textbook*, Longmans 1958.
- [22] K. Endo, T. Ohoyama, and R. Kimura. 1964, On the magnetic moment of Mn in aluminum Heusler alloy. *Journal of the Physical Society of Japan*, 19:1494–149
- [23]- Sanvito , Corey Oses, Junkai Xue, Anurag Tiwari, Mario Zic, Thomas Archer, *Science Advanced* 2017, 3: e1602241, 14 April 2017.